INSTITUT FÜR
MECHANIK UND
MECHATRONIK

Mechanics & Mechatronics

Diplomarbeit

Coupled Catenary and Pantograph dynamics on a small-scale moving domain

ausgeführt zum Zwecke der Erlangung des akademischen Grades eines Diplom-Ingenieurs
unter der Leitung von

Univ.Prof. Dr. Stefan Jakubek
Institut für Mechanik und Mechatronik
E325 A5

eingereicht an der Technischen Universität Wien

Fakultät für Maschinenwesen und Betriebswissenschaften

von

Daniel Ritzberger
Matr.Nr.: 0825912
Pilgramgasse 17/Top41
1050 Wien

Wien, am 4. März 2015

_____
Daniel Ritzberger

Eidesstattliche Erklärung

Ich erkläre eidesstattlich, dass ich die Arbeit selbständig angefertigt, keine anderen als die angegebenen Hilfsmittel benutzt und alle aus ungedruckten Quellen, gedruckter Literatur oder aus dem Internet im Wortlaut oder im wesentlichen Inhalt übernommenen Formulierungen und Konzepte gemäß den Richtlinien wissenschaftlicher Arbeiten zitiert, durch Fußnoten gekennzeichnet bzw. mit genauer Quellenangabe kenntlich gemacht habe.

Wien, am 4. März 2015   Daniel Ritzberger

Abstract

In this work, a novel approach for the simulation of the railway catenary and pantograph dynamics is proposed. The partial differential equations describing the vertical motion of the contact and carrier wires of the catenary are transformed in such a way that the pantograph is at rest with respect to the new moving coordinate. The computational domain is then truncated and absorbing boundary conditions are applied. High computational performance due to a great reduction in variables is achieved. The differences between this small scale system and a reference system with a fixed catenary length and a moving pantograph are investigated.

Contents

List of Figures

Chapter 1

Introduction

Figure 1.1: System Catenary/ Pantograph, taken from [1]

A numerical simulation of the complex catenary and pantograph dynamics (see Fig. 1.1) can give a better insight on how they interact with one another and lead to better design rules for the pantograph to prevent contact loss and electric arcing. The dynamics are described by coupled partial differential equations (PDEs). The classical approach for modelling the pantograph and catenary interaction [1] [3] considers a resting catenary and a moving pantograph. This formulation is also predominant in recent work studying more complex phenomena like wind disturbances and co-simulation of multi-body pantograph models [4]. For real-time applications a simplified mathematical model at the expense of simulation accuracy can be obtained by using the modal superposition principle [5] [6]. In the resting catenary formulation, the maximal simulation time is limited by the length of the catenary and the speed of the train. Longer simulations consequently increase the number of variables of the dynamical system and the computational effort. Moreover, spurious reflections occur if the pantograph is currently moving near the boundary. These unphysical reflections decrease the quality of the simulation and directly disturb the pantograph-catenary-interaction. A new approach that resolves these problems is presented here.

In this work a new formulation for the problem is introduced with the goals to

  i) make the size of the computational domain independent from the simulation time, and

  ii) reduce the computational effort so that the simulation can be carried out in

real-time without oversimplifying the underlying complex dynamic system.

This is achieved by a transformation of the PDEs which describe the catenary dynamics, to moving coordinates. The pantograph now remains at a fixed location with respect to the new coordinate and the catenary moves over the pantograph through the computational domain. To eliminate the disturbances due to reflections at the boundaries, absorbing boundary conditions (ABCs) are introduced which ideally let waves leave the computational domain without reflections. Thus, the length of this system can be chosen reasonably small, reducing the number of variables to be calculated. Using the transformed equations with a fixed pantograph an "endless" catenary is approximated on a bounded computational domain.

1.1 Organization

In chapter 2 the fundamentals used in this work are explained. First the PDEs describing the vertical movement of an Euler-Bernoulli beam, which will be used to model the catenary, as well as their discretization will be discussed. A numerical solver algorithm is devised. Next, an overview of absorbing boundary conditions and the perfectly matched layer formulation is given and their advantages and disadvantages are discussed. In chapter 3 the complete system description is assembled and the computational loop will be explained in detail. Chapter 4 gives a comparison between the moving system formulation and a traditional non-moving reference system. The model accuracy as well as the computation time are investigated.

Chapter 2

Fundamentals

2.1 Equations of motion for the Euler-Bernoulli beam

The Euler-Bernoulli-Beam equation with axial tensile load and fixed coordinates is given by

$$\rho A \frac{\partial^2 w(x,t)}{\partial t^2} + \beta \frac{\partial w(x,t)}{\partial t} = -EI \frac{\partial^4 w(x,t)}{\partial x^4} + T \frac{\partial^2 w(x,t)}{\partial x^2} + f(x,t) \tag{2.1}$$

Thereby, $w(x,t)$ is the displacement field of the beam, ρA is the beam mass per unit length, β the damping constant, EI the bending stiffness, T the tensile axial force and $f(x,t)$ is the vertical force density. This PDE is used to describe the transversal motion of the contact and carrier wires of the catenary.

Since the desired problem formulation is to be expressed with respect to a moving coordinate, so that the pantograph remains at a fixed center coordinate, the Euler-Bernoulli beam equation has to be transformed. In the following, the transformation is described as well as the methods used to obtain a numerical solution.

2.1.1 Transformation to moving coordinates

Equation (2.1) is transformed using a new coordinate $\hat{x}(t) = x + vt$ where v is the constant and sub-critical pantograph speed. Because $\frac{\partial \hat{x}}{\partial x} = 1$, the spatial partial derivatives, $\frac{\partial^n w(x(t),t)}{\partial x^n} = \frac{\partial^n w(\hat{x}(t),t)}{\partial \hat{x}^n}$, remain simple. The new coordinate is time-dependent, which has to be considered for the partial derivative with respect to t. Using implicit differentiation one obtains

$$\frac{dw(\hat{x}(t),t)}{dt} = \frac{\partial w(\hat{x},t)}{\partial t} - v \frac{\partial w(\hat{x},t)}{\partial \hat{x}} \tag{2.2}$$

and

$$\frac{d^2 w(\hat{x}(t),t)}{dt^2} = \frac{\partial^2 w(\hat{x},t)}{\partial t^2} - 2v \frac{\partial^2 w(\hat{x},t)}{\partial \hat{x} \partial t} + v^2 \frac{\partial^2 w(\hat{x},t)}{\partial \hat{x}^2} \tag{2.3}$$

Inserting (2.2) and (2.3) into (2.1) leads to the following equation of motion for a pretensioned Euler-Bernoulli beam with respect to a moving spatial coordinate.

$$\rho A\ddot{w} + \beta\dot{w} = -EIw'''' + (T - \rho Av^2)w'' + \beta vw' + 2v\rho A\dot{w}' + f(\hat{x}, t) \qquad (2.4)$$

To keep the notation simple the abbreviations $\frac{\partial w}{\partial t} = \dot{w}$ and $\frac{\partial w}{\partial \hat{x}} = w'$ are used, with higher order of derivatives respectively. Note that the transformed equation of motion now contains the mixed derivative $\dot{w}'$.

2.1.2 Boundary and initial conditions

In order to obtain a unique solution for Eq. (2.4), initial and boundary conditions have to be imposed. Since (2.4) is of second-order in time, two initial conditions are required, e.g.

$$w(\hat{x}, 0) = f(\hat{x}) \qquad (2.5)$$

$$\frac{\partial w(\hat{x}, 0)}{\partial t} = g(\hat{x}) \qquad (2.6)$$

The equations above specify the displacement and velocity fields at $t = 0$. Since the solution $w(\hat{x}, 0)$ is continuous in space, the initial conditions $f(x)$ and $g(x)$ are a function subjected to x. For the boundaries of the computational domain, there are several conditions that can be applied. For instance

$$w(0, t) = c_1 \qquad (2.7)$$
$$w(L, t) = c_2$$

In the equations above, L denotes the length of the computational domain ($0 \leq x \leq L$). The displacement w at boundary position is pinned to a fixed value $c_{1,2}$ for all time instances. This type of boundary condition are called Dirichlet boundary conditions. One can also specify the spatial derivative at boundary positions (Neumann boundary conditions)

$$\frac{\partial w(0, t)}{\partial \hat{x}} = c_3 \qquad (2.8)$$
$$\frac{\partial w(L, t)}{\partial \hat{x}} = c_4$$

If the solution of the PDE is of periodic nature, periodic boundary conditions can be applied.

$$w(0,t) = w(L,t) \tag{2.9}$$
$$\frac{\partial w(0,t)}{\partial \hat{x}} = \frac{\partial w(L,t)}{\partial \hat{x}}$$

With periodic boundary conditions, both boundaries are directly influenced by each other. For a PDE describing a wave motion this means, that a wave exiting the domain on one side is entering it on the other side. Later on, periodic boundary conditions are used when calculating the static displacement of one span of the endless catenary, since the displacement field outside of the computational domain is an endless periodic sequence of the same static displacement.

With Neumann and Dirichlet boundary conditions applied, waves are totally reflected at the boundary. Another type of boundary conditions which are designed to let waves leave the computational domain without reflections are absorbing boundary conditions (ABCs). These are discussed in chapter 2.3.

2.1.3 Discretizing the equations of motion

In order to obtain a numerical solution for the equation of motion of the axially loaded Euler-Bernoulli beam with respect to moving coordinates, various methods can be applied. For its simplicity a full-discrete finite difference approximation was chosen. For a full discussion on finite difference methods and their applications to wave equations see [7], [8].

In Eq. (2.4) the partial derivatives with respect to time and space are replaced by the corresponding central finite difference approximations.

$$
\begin{aligned}
\frac{\partial w(\hat{x},t)}{\partial t} &\approx \frac{w_n^{j+1} - w_n^{j-1}}{2\Delta t} \\
\frac{\partial^2 w(\hat{x},t)}{\partial t^2} &\approx \frac{w_n^{j+1} - 2w_n^j + w_n^{j-1}}{\Delta t^2} \\
\frac{\partial^2 w(\hat{x},t)}{\partial \hat{x}^2} &\approx \frac{w_{n+1}^j - 2w_n^j + w_{n-1}^j}{\Delta x^2} \\
\frac{\partial^4 w(\hat{x},t)}{\partial \hat{x}^4} &\approx \frac{w_{n+2}^j - 4w_{n+1}^j + 6w_n^j - 4w_{n-1}^j + w_{n-2}^j}{\Delta x^4} \\
\frac{\partial^2 w(\hat{x},t)}{\partial \hat{x} \partial t} &\approx \frac{w_{n+1}^{j+1} - w_{n+1}^{j-1} - w_{n-1}^{j+1} + w_{n-1}^{j-1}}{4\Delta x \Delta t}
\end{aligned}
\tag{2.10}
$$

In the difference approximations above, Δt denotes the temporal step size and Δx the spatial step size. By discretizing the PDE, the displacement field is no longer continuous. It is only defined at a finite number of discrete points in time and space. Smaller temporal and spatial step sizes generate a finer mesh for a given length of the beam and simulation time span, thereby increasing the number of discrete nodes that have to be calculated. This typically improves the accuracy of the numerical solution but also increases computational effort. To emphasize the fact that the
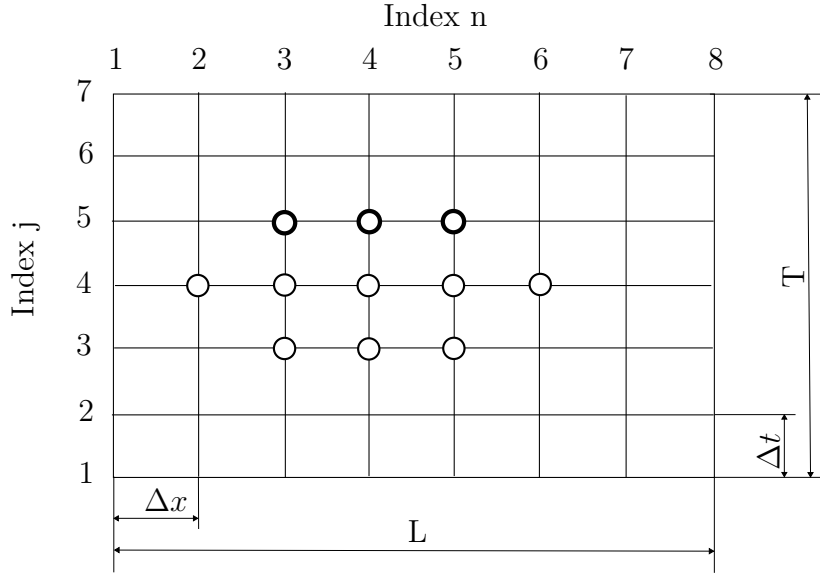
Figure 2.1: Interior stencil when central differences are used.

displacement field is now discrete, the notation $w_n^j \approx w(n\Delta x, j\Delta t)$ is introduced. This is the approximated value of the continuous displacement field at the node with time index j and space index n. When the finite difference approximations (2.10) are inserted into (2.4), the following algebraic equation is obtained.

$$\mathbf{a}^T \begin{pmatrix} w_{n-1}^{j+1} \\ w_n^{j+1} \\ w_{n+1}^{j+1} \end{pmatrix} = \mathbf{b}^T \begin{pmatrix} w_{n-2}^j \\ w_{n-1}^j \\ w_n^j \\ w_{n+1}^j \\ w_{n+2}^j \end{pmatrix} + \mathbf{c}^T \begin{pmatrix} w_{n-1}^{j-1} \\ w_n^{j-1} \\ w_{n+1}^{j-1} \end{pmatrix} + f_n^j \tag{2.11}$$

The row vectors $\mathbf{a}^T$, $\mathbf{b}^T$ and $\mathbf{c}^T$ in equation (2.11) contain the constant parameters of the Euler-Bernoulli-beam equation:

$$\mathbf{a}^T = \begin{pmatrix} \frac{v\rho A}{2\Delta x \Delta t} & \frac{\rho A}{\Delta t^2} + \frac{\beta}{2\Delta t} & -\frac{v\rho A}{2\Delta x \Delta t} \end{pmatrix} \tag{2.12}$$

$$\mathbf{b}^T = \begin{pmatrix} -\frac{EI}{\Delta x^4} & 4\frac{EI}{\Delta x^4} + \frac{T-\rho Av^2}{\Delta x^2} & -6\frac{EI}{\Delta x^4} - 2\frac{T-\rho Av^2}{\Delta x^2} + 2\frac{\rho A}{\Delta t^2} & 4\frac{EI}{\Delta x^4} + \frac{T-\rho Av^2}{\Delta x^2} & -\frac{EI}{\Delta x^4} \end{pmatrix} \tag{2.13}$$

$$\mathbf{c}^T = \begin{pmatrix} \frac{v\rho A}{2\Delta x \Delta t} & \frac{\rho A}{\Delta t^2} - \frac{\beta}{2\Delta t} & -\frac{v\rho A}{2\Delta x \Delta t} \end{pmatrix} \tag{2.14}$$

Eq. (2.11) has to be evaluated for every discrete node and it turns out, that each node is dependent to its neighbouring nodes due to the difference approximation. In Fig. 2.1 this dependency is illustrated. The graphical representation of these algebraic

dependencies is called stencil. Because the mixed derivative term in Eq. (2.4) was also discretized using central finite differences, the solution of a node at the next time step w_n^{j+1} cannot be explicitly computed. It also depends on its neighbouring nodes at the next time step w_{n-1}^{j+1} and w_{n+1}^{j+1}. Therefore, the displacement field at the next time step has to be solved implicitly for every node at once. For that, Eq. (2.11) is formulated for the entire spatial domain:

$$\mathbf{A}\mathbf{w}^{j+1} = \mathbf{B}\mathbf{w}^j + \mathbf{C}\mathbf{w}^{j-1} + \mathbf{f}^j \tag{2.15}$$

where

$$\mathbf{A} = \begin{pmatrix} \ddots & & & \\ & \mathbf{a}^T & & \mathbf{0} \\ & & \mathbf{a}^T & \\ & \mathbf{0} & & \mathbf{a}^T \\ & & & & \ddots \end{pmatrix}, \mathbf{B} = \begin{pmatrix} \ddots & & & \\ & \mathbf{b}^T & & \mathbf{0} \\ & & \mathbf{b}^T & \\ & \mathbf{0} & & \mathbf{b}^T \\ & & & & \ddots \end{pmatrix} \tag{2.16}$$

$$\mathbf{C} = \begin{pmatrix} \ddots & & & \\ & \mathbf{c}^T & & \mathbf{0} \\ & & \mathbf{c}^T & \\ & \mathbf{0} & & \mathbf{c}^T \\ & & & & \ddots \end{pmatrix} \tag{2.17}$$

and

$$\mathbf{w}^{j+1} = \begin{pmatrix} \vdots \\ w_{n-1}^{j+1} \\ w_n^{j+1} \\ w_{n+1}^{j+1} \\ \vdots \end{pmatrix}, \mathbf{w}^j = \begin{pmatrix} \vdots \\ w_{n-1}^j \\ w_n^j \\ w_{n+1}^j \\ \vdots \end{pmatrix}, \mathbf{w}^{j-1} = \begin{pmatrix} \vdots \\ w_{n-1}^{j-1} \\ w_n^{j-1} \\ w_{n+1}^{j-1} \\ \vdots \end{pmatrix}, \mathbf{f}^j = \begin{pmatrix} \vdots \\ f_{n-1}^j \\ f_n^j \\ f_{n+1}^j \\ \vdots \end{pmatrix} \tag{2.18}$$

As can be seen from Fig. 2.1, additional information is needed when the interior stencil reaches the spatial boundary of the computational domain for the non-existing nodes outside of the domain. Suitable boundary conditions are necessary. The values for the nodes outside of the boundary are either known (Dirichlet boundary condition) or dependent on other nodes (Neumann, periodic, or absorbing boundary conditions).

To avoid dependencies on nodes outside of the computational domain, the stencils near the boundary can be modified such that no information outside of the boundary is needed. This is achieved by using asymmetric forward or backwards difference approximations for the spatial derivatives. Fig. 2.2 illustrates the central and the asymmetric stencils at the boundary. Having a different finite difference approximation scheme at the boundary leads to altered $\mathbf{a}^T$, $\mathbf{b}^T$ and $\mathbf{c}^T$ row vectors for the
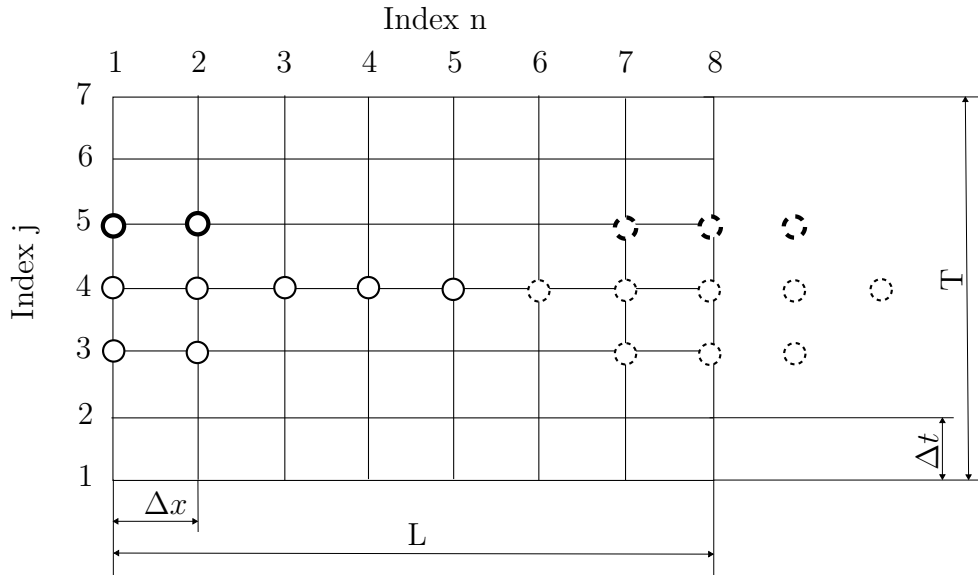
Figure 2.2: Boundary stencil with asymmetric difference approximation (left) and central difference approximation (right).

corresponding rows in Eq. (2.15). This modification did not eliminate the need for boundary conditions, because Eq. (2.15) is ill-posed without boundary conditions, meaning that no unique solution can be obtained.

The boundary conditions are then implemented by substituting the first and last row in (2.15) with the discretized boundary condition equation. The displacement field at the next time step $\mathbf{w}_n^{j+1}$ can now be solved by inverting matrix $\mathbf{A}$.

$$\mathbf{w}^{j+1} = \mathbf{A}^{-1}\mathbf{B}\mathbf{w}^j + \mathbf{A}^{-1}\mathbf{C}\mathbf{w}^{j-1} + \mathbf{A}^{-1}\mathbf{f}^j \tag{2.19}$$

This is a simple time marching solver. With the discrete form of the initial conditions (2.5)–(2.6) the solver can be started and continued for any desired amount of time steps, assuming that the force density vector $\mathbf{f}^j$ is known. The matrix inversion $\mathbf{A}^{-1}$ requires a great computational effort. Calculating the inverse every time step would drastically slow down the solver, but since the matrix $\mathbf{A}$ is time-invariant, the inverse can be calculated and stored once at the beginning of the solving process.

2.2 Fundamental solution and dispersion relation

For a detailed discussion about wave equations, their fundamental solutions and dispersion relation see [9], [10]. The complex fundamental solution of a PDE describing wave motion is given by

$$w(x,t) = e^{i\omega_x x}e^{i\omega_t t}, \tag{2.20}$$

where ω_t is the angular frequency, ω_x the wave number and i the imaginary unit. The group velocity v_g is defined as

$$v_g = -\frac{\partial \omega_t}{\partial \omega_x} \tag{2.21}$$

and the phase velocity v_p as

$$v_p = -\frac{\omega_t}{\omega_x} \tag{2.22}$$

The phase velocity is the speed at which a fundamental wave with a certain wave number and angular frequency propagates through space, whereas the group velocity is the propagation speed of the envelope of a wave package containing several fundamental waves of neighbouring frequencies. The relation of angular frequency ω_t and wave number ω_x is given by the dispersion relation. It is derived by inserting the fundamental solution (2.20) into the wave equation. For demonstration purposes, this procedure is shown for the scalar wave equation

$$\frac{\partial^2 w}{\partial t^2} = c^2 \frac{\partial^2 w}{\partial x^2}. \tag{2.23}$$

Inserting (2.20) into (2.23) leads to the dispersion relation

$$\omega_t^2 = c^2 \omega_x^2. \tag{2.24}$$

From this equation, the group and phase velocity can be calculated,

$$v_g = v_p = \pm c. \tag{2.25}$$

The group and the phase velocity is the same and, furthermore, the phase velocity is constant for all wave numbers. This means that the continuous scalar wave equation is dispersion-free. Now the dispersion relation for the discrete scalar wave equation is investigated. The partial derivatives are substituted with their central finite difference approximations.

$$w_n^{j+1} - 2w_n^j + w_n^{j-1} = c^2 \frac{\Delta t^2}{\Delta x^2}(w_{n+1}^j - 2w_n^j + w_{n-1}^j) \tag{2.26}$$

The discrete fundamental solution is written as

$$w_n^j = \underbrace{e^{i\omega_x \Delta x n}}_{\kappa^n}\underbrace{e^{i\omega_t \Delta t j}}_{\tau^j}. \tag{2.27}$$

Inserted into the discrete wave equation the following relation is obtained:

$$\tau - 2 + \tau^{-1} = c^2 \frac{\Delta t^2}{\Delta x^2}(\kappa - 2 + \kappa^{-1}) \tag{2.28}$$

With

$$\tau + \tau^{-1} = 2\cos(\omega_t \Delta t)$$
$$\kappa + \kappa^{-1} = 2\cos(\omega_x \Delta x) \tag{2.29}$$

and

$$2\cos(\omega_t \Delta t) - 2 = -4sin\left(\frac{\omega_t \Delta t}{2}\right)^2$$
$$2\cos(\omega_x \Delta x) - 2 = -4sin\left(\frac{\omega_x \Delta x}{2}\right)^2 \tag{2.30}$$

inserted into (2.28), the discrete dispersion relation for the scalar wave equation is

$$sin\left(\frac{\omega_t \Delta t}{2}\right)^2 = c^2 \frac{\Delta t^2}{\Delta x^2} sin\left(\frac{\omega_x \Delta x}{2}\right)^2. \tag{2.31}$$

It can be seen that when the quantities Δx and Δt are small, (2.31) approximates (2.24). Furthermore, if

$$\frac{\Delta x}{\Delta t} = c \tag{2.32}$$

the discrete dispersion relation is equal to the continuous dispersion relation. If the ratio between the spatial and temporal grid size is not equal to the wave speed, then the phase speed is a function of ω_x and substantial dispersion due to the discretization occurs.

An infinite set of frequency pairs (ω_x, ω_t) exists, but the quantities $\omega_x \Delta x$ and $\omega_t \Delta t$ of the discrete fundamental solution can be confined to the interval $[-\pi, \pi]$. This can be seen by investigating a standing wave

$$w_n = e^{i\omega_x \Delta x n} = cos(\omega_x \Delta x n) + i\sin(\omega_x \Delta x n). \tag{2.33}$$

If $\omega_x \Delta x = \pm\pi$ the imaginary term in (2.33) is equal to zero and $cos(\pi n)$ is ± 1 for all n; the standing wave is a sawtooth. All higher quantities $\omega_x \Delta x > \pm\pi$ result in a wave that can not be resolved by the grid and gives rise to aliasing.

To obtain the discrete dispersion relation for the moving Euler-Bernoulli beam, the same technique as described above can be used. When inserting the fundamental solution (2.27) into the discretized equation of motion (2.11), and using the relations (2.29)–(2.30) the discrete dispersion relation

$$\sin\left(\frac{\omega_t \Delta t}{2}\right)^2 = \left(\frac{T}{\rho A} - v^2\right)\frac{\Delta t^2}{\Delta x^2}\sin\left(\frac{\omega_x \Delta x}{2}\right)^2 + \frac{EI\Delta t^2}{\rho A \Delta x^4}\left(4\sin\left(\frac{\omega_x \Delta x}{2}\right)^2 - \sin(\omega_x \Delta x)^2\right)$$
$$+ \frac{v\Delta t}{2\Delta x}\sin(\omega_t \Delta t)\sin(\omega_x \Delta x) \tag{2.34}$$

is obtained. When deriving this equation, damping was neglected. The dispersion
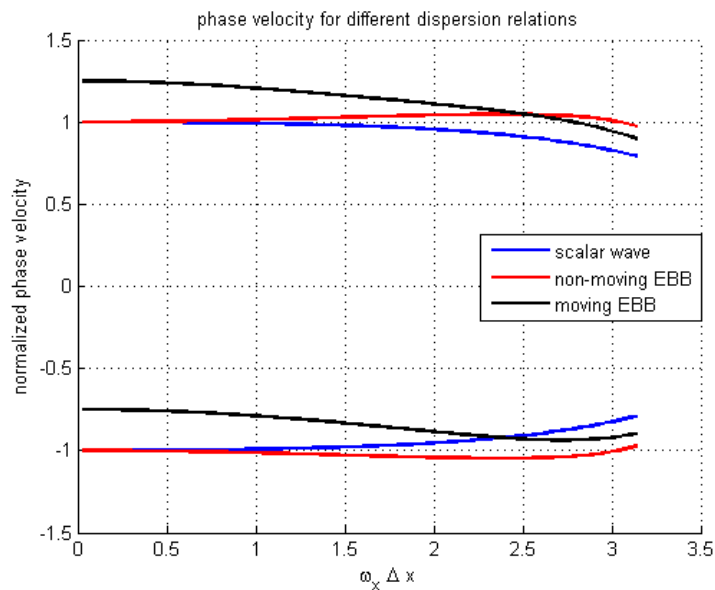
Figure 2.3: Normalized phase velocity for the scalar wave equation (blue),
           the non-moving Euler-Bernoulli beam (red) and the moving
           Euler-Bernoulli beam (black) for $v = 0.25c$

relation for the non-moving Euler-Bernoulli beam is also contained in (2.34) and obtained by setting the velocity of the moving coordinate system v to zero. Unlike the scalar wave equation, where dispersion only occurs due to discretization, the Euler-Bernoulli beam has also physical dispersion because of the bending stiffness EI.

In Fig. 2.3, the normalized phase velocity for the scalar wave equation, the non-moving Euler-Bernoulli beam and the moving Euler-Bernoulli beam is plotted over $\omega_x \Delta x$. There are two branches for the phase velocity, since there are left- and right-going waves. The grid speed (2.32) was set to $0.9c$ causing dispersion for the discrete scalar wave equation. It can be seen that waves with a low wave number travel at a speed close to c, but for higher wave numbers, the phase velocity decreases substantially. For the non-moving Euler-Bernoulli beam, the phase velocity increases with $\omega_x \Delta x$, causing waves with a high wave number to travel faster. For the scalar wave equation and the non-moving EBB, the two phase velocity branches are symmetrical around zero. This is not the case for the moving EBB, since the phase speed is reduced when travelling in the same direction as the moving coordinate system and increased when moving in the opposite direction.

2.3 Absorbing boundary conditions

When computing the solution of an unbounded wave equation with a spatially discretizing method, the computational domain has to be truncated at finite lengths

due to computational limitations, mainly computation speed and limited memory. If the solution of this domain with fixed length should approximate the free space solution of infinite length, absorbing boundary conditions are required. Ideally, those let waves leave the computational domain without reflections. An analytic approach for deriving ABCs is given by [11]. Discrete ABC formulations and its stability is discussed in detail in [12] and [10].

In this chapter, the analytic construction mechanism of ABCs for the two-dimensional wave equation, the simplified one-dimensional case and its limitations are discussed. With the two-dimensional wave equation

$$\frac{\partial^2 w}{\partial t^2} = \frac{\partial^2 w}{\partial x^2} + \frac{\partial^2 w}{\partial y^2}, \tag{2.35}$$

where the wave speed is scaled to 1, and its fundamental solution

$$w(t, x, y) = e^{i(\omega_t t + \omega_x x + \omega_y y)}, \tag{2.36}$$

we obtain the continuous dispersion relation

$$\omega_t^2 = \omega_x^2 + \omega_y^2 \tag{2.37}$$

or

$$\omega_x = \pm\, \omega_t \sqrt{1 - s^2}$$
$$s = \frac{\omega_y}{\omega_t} \tag{2.38}$$

In this equation, the sign coming from the square root determines if a left- or a right-going wave is to be considered (e.g. constructing ABCs for the left or right boundary). The positive one-way dispersion relation

$$\omega_x = \omega_t \sqrt{1 - s^2} \tag{2.39}$$

is that of a pseudodifferential equation, and therefore can not directly be converted back to a differential equation, because of the square root. To make the conversion possible, a Padé approximation of the square root is used

$$1st\ order: \quad \sqrt{1 - s^2} \approx 1$$
$$2nd\ order: \quad \sqrt{1 - s^2} \approx 1 - \frac{1}{2}s^2 \tag{2.40}$$

which leads to the following ABCs

$$1st\ order: \quad \frac{\partial w}{\partial x} = \frac{\partial w}{\partial t}$$
$$2nd\ order: \quad \frac{\partial^2 w}{\partial x \partial t} = \frac{\partial^2 w}{\partial t^2} - \frac{1}{2}\frac{\partial^2 w}{\partial y^2} \tag{2.41}$$

When deriving ABCs for the one-dimensional wave equation in the same way, there is no square root that has to be approximated so they can be formulated exactly. Doing

so leads to ABCs which are the same as the first order approximation of the two-dimensional wave equation (since approximating the square root with $\sqrt{1 - s^2} \approx 1$ leads to the one-dimensional dispersion relation).

So, for the one-dimensional wave equation we obtain the ABCs

$$\dot{w} = \pm c w' \tag{2.42}$$

Since these conditions were derived from the continuous dispersion relation, where the phase velocity is constant, they typically do not absorb waves perfectly when the wave equation and the ABCs are discretized. As seen in Chapter 2.2, when discretizing the wave equation, numerical dispersion occurs resulting in lower phase velocities for higher wave numbers. Waves with a low wave number travel with a speed close to c and are reasonably well absorbed, but the higher the difference between the actual phase velocity of a wave with a certain wave number and c, the greater the reflections are. Perfect absorption for all wave numbers can only be achieved when relation (2.32) holds, since then the discrete and the continuous dispersion relation, for which the ABCs were constructed, are equal. When these ABCs are imposed on the Euler-Bernoulli beam, where dispersion is always present, again only waves with a low wave number are absorbed well.

2.4 Perfectly matched layer

The key idea of the perfectly matched layer (PML) is to surround the computational domain with an additional layer of finite thickness which absorbs waves entering it. This is achieved by altering the fundamental solution inside the PML and translating this modification of the fundamental solution back to a corresponding partial differential equation. To make sure that no reflections occur at the interface between the PML and the computational core domain, the fundamental solution inside the PML and the fundamental solution of the computational domain have to be the continuous at the interface (perfectly matched). PMLs were first derived for electro-magnetic waves (see [13]) where the wave equations are given in a split-field formulation. A full discussion of PMLs is given by [14], [2].

Once again, the fundamental solution for the one-dimensional wave equation

$$w(x,t) = e^{i\omega_x x} e^{i\omega_t t} \tag{2.43}$$

is considered. When evaluating it along a real-valued coordinate x, an oscillating solution is obtained. Evaluating the fundamental solution along a complex contour $\tilde{x} = x + i f(x)$ results in

$$w(\tilde{x},t) = e^{i\omega_x(x+if(x))} e^{i\omega_t t} = e^{-\omega_x f(x)} \underbrace{e^{i\omega_x x} e^{i\omega_t t}}_{w(x,t)}. \tag{2.44}$$

Note, that when $f(x)$ is zero, one obtains the original fundamental solution, whereas if $f(x)$ is > 0, which defines the imaginary part of the complex contour $\tilde{x}$, an expo-
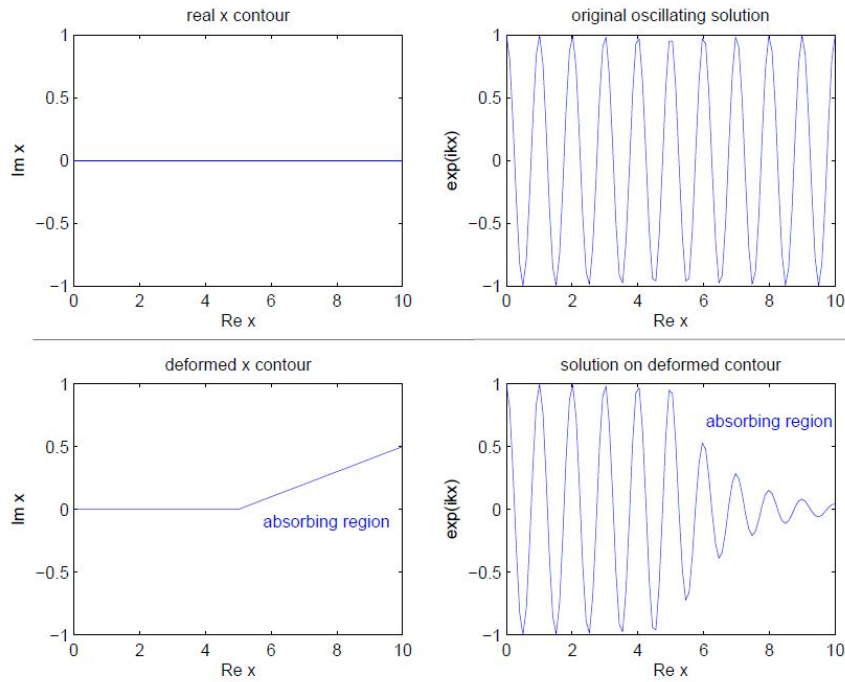
Figure 2.4: Top: oscillatory fundamental solution when evaluated at a real x contour. Bottom: The function $f(x)$ linearly increases for $x > 5$ (absorbing region) and zero for $x \leq 5$ resulting in exponential decay inside the PML region. Taken from [2]

nential decay in space is added to the fundamental solution. This can be seen in Fig. 2.4. The solution inside the computational domain is unchanged and continuous at the interface, therefore no reflections occur.

Since the complex coordinate $\tilde{x}$ is time invariant, $\frac{\partial w(x,t)}{\partial t} = \frac{\partial w(\tilde{x},t)}{\partial t}$ holds. Furthermore, $\frac{\partial w(x,t)}{\partial x} = \frac{\partial w(\tilde{x},t)}{\partial \tilde{x}}$ and, lastly, because the wave equation is invariant in x, the fundamental solution evaluated at a complex contour satisfies the same partial differential equation with respect to the complex coordinate.

$$\frac{\partial^2 w}{\partial t^2} = \frac{\partial^2 w}{\partial \tilde{x}^2} \tag{2.45}$$

Since the partial differential equation with respect to a complex variable cannot easily be solved, it is desired to transform the equation back to its original real-valued coordinate x.

$$\partial \tilde{x} = \Big(1 + i\frac{df(x)}{dx}\Big)\partial x \longrightarrow \frac{\partial}{\partial \tilde{x}} = \frac{\partial}{\Big(1 + i\frac{df(x)}{dx}\Big)\partial x} \tag{2.46}$$

With the relation above, Eq. (2.45) can be transformed. Before investigating the transformation it is useful to define a suitable function $f(x)$. Since in the coordinate

transformation (2.46) only the derivative of the function $f(x)$ is to be found, it seems advantageous to formulate

$$f(x) = -\frac{1}{\omega_t} \int_0^x \sigma(\xi) d\xi \qquad (2.47)$$

The function σ is called the damping profile. With a damping profile $\sigma = const.$ a complex contour as in Fig. 2.4 is obtained. The scaling $-\frac{1}{\omega_t}$ is chosen because the exponential decay of the fundamental solution

$$e^{-\omega_x f(x)} = e^{\frac{\omega_x}{\omega_t} \int_0^x \sigma(\xi) d\xi} = e^{-\frac{1}{v_p} \int_0^x \sigma(\xi) d\xi} \qquad (2.48)$$

now contains $\frac{\omega_x}{\omega_t}$, the inverse of the phase velocity v_p, which is constant for non-dispersive wave equations. This results in a constant decay for all fundamental waves independent of their wave number ω_x. If this scaling was not done, a high decay rate is only achieved for high wave numbers. One way to perform the transformation is realized by writing (2.45) in a split-field formulation

$$\frac{\partial w}{\partial t} = \frac{\partial v}{\partial \tilde{x}} \qquad (2.49)$$

$$\frac{\partial v}{\partial t} = \frac{\partial w}{\partial \tilde{x}} \qquad (2.50)$$

where w is the original displacement field and v an auxiliary field. Performing the transformation in the split-field formulation gives an advantage as will be seen later, but it introduces an additional artificial field. Now the transformation (2.46) with the defined function $f(x)$ is applied.

$$\frac{\partial w}{\partial t} = i\omega_t w = \frac{\partial v}{\partial x} \frac{1}{(1 - \frac{i}{\omega_t}\sigma(x))} \qquad (2.51)$$

$$\frac{\partial v}{\partial t} = i\omega_t v = \frac{\partial w}{\partial x} \frac{1}{(1 - \frac{i}{\omega_t}\sigma(x))} \qquad (2.52)$$

Multiplying by $(1 - \frac{i}{\omega_t}\sigma(x))$ leads to

$$i\omega_t w + \sigma(x)w = \frac{\partial w}{\partial t} + \sigma(x)w = \frac{\partial v}{\partial x} \qquad (2.53)$$

$$i\omega_t v + \sigma(x)v = \frac{\partial v}{\partial t} + \sigma(x)v = \frac{\partial w}{\partial x} \qquad (2.54)$$

which are the equations for the PML in split-field formulation. Again, inside the computational domain where $\sigma(x) = 0$ the solution is unchanged.

For an unsplit PML formulation, consider the wave equation (2.45). Using the trans-

formation (2.46) with $f(x)$ defined as in (2.47) yields

$$\frac{\partial^2 w}{\partial t^2} = \frac{\partial\left(\frac{\partial w}{\partial x}\frac{\omega_t}{\omega_t - i\sigma(x)}\right)}{\partial x}\frac{\omega_t}{\omega_t - i\sigma(x)} \tag{2.55}$$

Because the damping profile is dependent on x, the partial differentiation leads to

$$\begin{aligned}
\ddot{w} &= \left[w''\frac{\omega_t}{\omega_t - i\sigma(x)} - w'\frac{\omega_t}{(\omega_t - i\sigma(x))^2}i\sigma'(x)\right]\frac{\omega_t}{\omega_t - i\sigma(x)} \\
&= \left[w'' - w'\frac{i\sigma'(x)}{\omega_t - i\sigma(x)}\right]\frac{\omega_t^2}{(\omega_t - i\sigma(x))^2}
\end{aligned} \tag{2.56}$$

To simplify the equation above, the shorthand notations for the partial derivatives are used. By looking at the fundamental solution it can be seen that the partial derivative with respect to time corresponds to

$$\dot{w} = i\omega_t w \tag{2.57}$$
$$\ddot{w} = -\omega_t^2 w \tag{2.58}$$

Inserted into (2.56) and rearranging the equation gives

$$-\omega_t^2 w + 2\sigma(x)i\omega_t w + \sigma(x)^2 w = w'' - \frac{iw'\sigma(x)}{\omega_t - i\sigma(x)} \tag{2.59}$$

The last step is to transform this equation in frequency domain back to its corresponding partial differential equation. If multiplied by the denominator of the second term on the right hand side, the corresponding partial differential equation would have a third order derivative with respect to time and mixed derivatives (this problem does not occur in the split-field formulation). If this is not wanted, an auxiliary field can be used.

$$-\omega_t^2 w + 2\sigma(x)i\omega_t w + \sigma(x)^2 w = w'' + \Phi \tag{2.60}$$

$$\Phi = -\frac{iw'\sigma(x)}{\omega_t - i\sigma(x)} \tag{2.61}$$

This set of equations can be related back to a corresponding set of partial differential equations

$$\ddot{w} + 2\sigma(x)\dot{w} + \sigma(x)^2 w = w'' + \Phi \tag{2.62}$$
$$\dot{\Phi} + \sigma(x)\Phi = w'\sigma'(x) \tag{2.63}$$

which is one possible unsplit PML formulation. There are many different possibilities of introducing an auxiliary field to the equation (2.59) to avoid additional derivatives of higher order, but some of these auxiliary fields tend to be unstable.

The continuous PML equations are perfectly absorbing, and the layer width can be chosen arbitrarily small by using a high-valued damping profile. When the equations are discretized this is not the case. If the damping profile would be chosen like in Fig. 2.4 the problem arises that $\sigma'(x)$ is a Dirac impulse at the interface. When computing $\sigma'(x)$ numerically this is only obtained for $\Delta x \longrightarrow 0$. To avoid numerical reflections at the interface, Δx should be chosen small and the damping profile $\sigma(x)$ to be of second or third order so that its derivative is continuous at the interface.

In [15] a perfectly matched layer is constructed for an elastically bedded Euler-Bernoulli beam. Essentially, the same techniques described above are used. To translate the frequency domain equation back to a corresponding PDE the forth-order derivative in space is cast into four equations with first-order derivatives (as it was done with the scalar wave equation above). Thus, the number of variables for the beam with PML region quadruples, which drastically increases the computational effort. Although the perfectly matched layer offers better absorption of waves in a dispersive medium than the absorbing boundary conditions, the increase in variables to be solved and the less straightforward implementation make this approach less suitable for real-time computation. Thus in the remainder of this work the absorbing boundary conditions are used.

Chapter 3

System description

In this chapter, the methodology discussed above will be used to assemble a model of the pantograph-catenary dynamics. As opposed to other formulations (see [3], [5]) the dynamics will be described with respect to a moving, pantograph-fixed, coordinate system. The catenary, which is now moving over the resting pantograph, is truncated at a length of one span (the spatial periodicity of the static solution). Absorbing boundary conditions are imposed to minimize unphysical reflections at the computational boundary so that the truncated catenary approximates an endless catenary. This formulation has the advantage that the simulation time can be arbitrarily chosen and does not influence the length of the system and therefore decreases the computational effort. This would not be the case if the dynamic model was given with respect to a resting coordinate system. Since then the pantograph moves along the catenary with a given velocity, the length of the system must be at least the size of the distance the pantograph travels during the simulation time and has to be increased even further for reflections at the boundary to not disturb the interaction between the pantograph and the catenary.
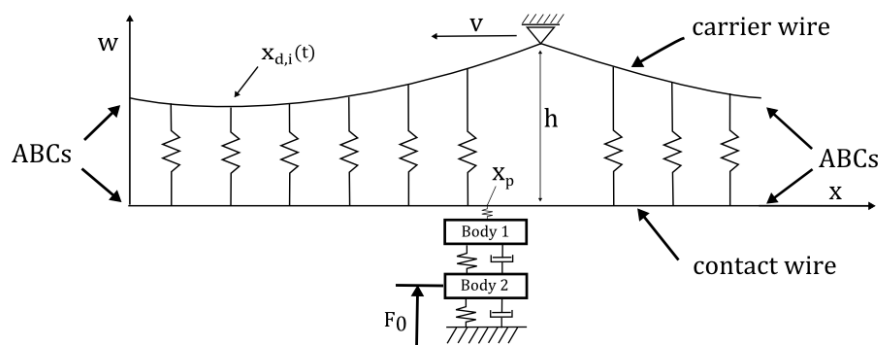

Figure 3.1: Catenary and Pantograph system description

The main disadvantage of this new formulation is that the dropper positions are time-dependent, and furthermore that the droppers enter and leave the computa-

tional domain. There is no information outside the computational domain and the discontinuous, sudden event of a dropper entering disturbs the dynamics. The same applies for the mast position.

3.1 Catenary dynamics

The model of the coupled catenary and pantograph dynamics is shown in Fig. 3.1. The catenary consists of the carrier wire and the contact wire. The carrier wire is held by masts at a fixed height of h. The distance between two subsequent masts l is also assumed as the periodicity of the catenary. The contact wire is suspended by droppers from the carrier wire. This results in a coupling of the contact and carrier wire dynamics. The lateral movement of the contact and carrier wire is described by the moving Euler-Bernoulli beam equation (2.4) which is discretized and aggregated into a state space system (2.15). For the contact and the carrier wire two separate state space systems are obtained.

$$\mathbf{A}_c \mathbf{w}_c^{j+1} = \mathbf{B}_c \mathbf{w}_c^j + \mathbf{C}_c \mathbf{w}_c^{j-1} + \mathbf{f}_c^j \tag{3.1}$$

$$\mathbf{A}_w \mathbf{w}_w^{j+1} = \mathbf{B}_w \mathbf{w}_w^j + \mathbf{C}_w \mathbf{w}_w^{j-1} + \mathbf{f}_w^j \tag{3.2}$$

Here, the subscript c denotes the displacement and the parameters for the carrier wire and w the displacement and parameters for the contact wires.

3.1.1 Applying absorbing boundary conditions

For its simplicity, the absorbing boundary conditions (2.41) are imposed at the boundary of the contact and carrier wire.

$$\dot{w} = \pm(c \mp v)w' \tag{3.3}$$

Again, since dispersion occurs for the Euler-Bernoulli beam, only waves with phase speed close to c are absorbed well. Because the wave motion is described with respect to a moving coordinate system, the phase speed of left-going waves is increased by v and for right-going waves decreased by v. This simple relationship only holds for waves with a low wave number (see Fig 2.3). The sign of the ABCs above determines if left- or right-going waves are to be absorbed (e.g. left or right boundary respectively). Discretizing the equations above leads to the left boundary condition

$$w_1^{j+1} = \left(1 - (c + v)\frac{\Delta t}{\Delta x}\right)w_1^j + (c + v)\frac{\Delta t}{\Delta x}w_2^j \tag{3.4}$$
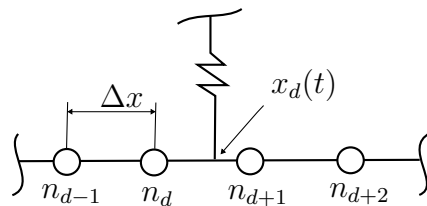
Figure 3.2: General position of the dropper in between two discrete nodes

and to the right boundary condition

$$w_{n_{max}}^{j+1} = \left(1 - (c-v)\frac{\Delta t}{\Delta x}\right)w_{n_{max}}^j + (c-v)\frac{\Delta t}{\Delta x}w_{n_{max}-1}^j \tag{3.5}$$

An asymmetric stencil was used near the boundary when discretizing the Euler-Bernoulli beam equation, so that the first and the last rows of the matrix equations (3.1)–(3.2) need to be substituted with the discrete ABCs (3.4)–(3.5). Note that due to different parameters the wave speed c is in general not the same for the contact and the carrier wires. The algebraic equations (3.1)–(3.2) can be written as

$$\begin{pmatrix}\mathbf{A}_c & \mathbf{0} \\ \mathbf{0} & \mathbf{A}_w\end{pmatrix}\begin{pmatrix}\mathbf{w}_c^{j+1} \\ \mathbf{w}_w^{j+1}\end{pmatrix} = \begin{pmatrix}\mathbf{B}_c & \mathbf{0} \\ \mathbf{0} & \mathbf{B}_w\end{pmatrix}\begin{pmatrix}\mathbf{w}_c^{j} \\ \mathbf{w}_w^{j}\end{pmatrix} + \begin{pmatrix}\mathbf{C}_c & \mathbf{0} \\ \mathbf{0} & \mathbf{C}_w\end{pmatrix}\begin{pmatrix}\mathbf{w}_c^{j-1} \\ \mathbf{w}_w^{j-1}\end{pmatrix} + \begin{pmatrix}\mathbf{f}_c^{j} \\ \mathbf{f}_w^{j}\end{pmatrix} \tag{3.6}$$

$$\mathbf{A}\mathbf{w}^{j+1} = \mathbf{B}\mathbf{w}^{j} + \mathbf{C}\mathbf{w}^{j-1} + \mathbf{f}^{j} \tag{3.7}$$

3.1.2 Adding dropper interaction

There are i droppers in a span coupling the vertical movement of the contact and the carrier wires. They are modelled as a spring, so the force acting on the wires at dropper position $x_{d,i}(t)$ is given by

$$F_{d,i} = k_{d,i}[w_c(x_{d,i}(t)) - w_w(x_{d,i}(t)) - l_{0,i}] \tag{3.8}$$

In this equation $k_{d,i}$ is the spring constant, $w_{c/w}(x_{d,i}(t))$ the displacement of the carrier and contact wire at the current dropper position and $l_{0,i}$ is the unstretched length of a dropper which is chosen as such that the static sag of the contact wire is minimal.

Note that the displacement of contact and carrier wires are only given at discrete points $w_{c/w}(\Delta x n)$ so that the current dropper position $x_d(t)$ in general lies in between two discrete nodes (see Fig. 3.2).

The displacements at dropper position $w_{c/w}(x_d)$ is approximated by a linear interpolation using the surrounding nodes

$$w(x_d) \approx w_{n_d} + \frac{w_{n_d+1} - w_{n_d}}{\Delta x}(x_d(t) - \Delta x n_d) \tag{3.9}$$

The equation above is applied for both contact and carrier wire. For the sake of clarity the subscript c/w was dropped in the equation above. When defining the membership ratio

$$\alpha = \frac{x_d(t) - \Delta x n_d}{\Delta x} \tag{3.10}$$

the interpolation can be rewritten as

$$w(x_d) \approx \begin{pmatrix} 1-\alpha & \alpha \end{pmatrix} \begin{pmatrix} w_{n_d} \\ w_{n_d+1} \end{pmatrix} \tag{3.11}$$

Inserting this into (3.8) leads to

$$F_d = k_d \left[\begin{pmatrix} 1-\alpha & \alpha \end{pmatrix} \begin{pmatrix} w_{c,n_d} \\ w_{c,n_d+1} \end{pmatrix} - \begin{pmatrix} 1-\alpha & \alpha \end{pmatrix} \begin{pmatrix} w_{w,n_d} \\ w_{w,n_d+1} \end{pmatrix} - l_0 \right] \tag{3.12}$$

The dropper force F_d acting between two discrete nodes is then linearly distributed to the surrounding nodes by again using the membership ratio

$$\begin{pmatrix} F_{d,n_d} \\ F_{d,n_d+1} \end{pmatrix} = \begin{pmatrix} 1-\alpha \\ \alpha \end{pmatrix} F_d \tag{3.13}$$

When defining a distribution vector

$$\phi = \begin{pmatrix} 1-\alpha \\ \alpha \end{pmatrix} \tag{3.14}$$

the distributed and interpolated dropper force can be written as

$$\begin{pmatrix} F_{d,n_d} \\ F_{d,n_d+1} \end{pmatrix} = k_d \phi \phi^T \begin{pmatrix} w_{c,n_d} \\ w_{c,n_d+1} \end{pmatrix} - k_d \phi \phi^T \begin{pmatrix} w_{w,n_d} \\ w_{w,n_d+1} \end{pmatrix} - k_d \phi l_0 \tag{3.15}$$

These forces are then divided by the spatial step size Δx to obtain the force density and then added to its corresponding force density entries $\mathbf{f}_c^j$ and $\mathbf{f}_w^j$ in (3.7) with a negative sign for the carrier wire and a positive sign for the contact wire.

$$
\begin{pmatrix} \vdots \\ f^j_{c,n_d} \\ f^j_{c,n_d+1} \\ \vdots \\ f^j_{w,n_d} \\ f^j_{w,n_d+1} \\ \vdots \end{pmatrix} = \frac{k_d}{\Delta x} \underbrace{\begin{pmatrix} \mathbf{0} & & & \\ & -\boldsymbol{\phi}\boldsymbol{\phi}^T & & \boldsymbol{\phi}\boldsymbol{\phi}^T \\ & & \mathbf{0} & \\ & \boldsymbol{\phi}\boldsymbol{\phi}^T & & -\boldsymbol{\phi}\boldsymbol{\phi}^T \\ & & & & \mathbf{0} \end{pmatrix}}_{\mathbf{B}^j_d} \begin{pmatrix} \mathbf{w}^j_c \\ \mathbf{w}^j_w \end{pmatrix} + \frac{k_d}{\Delta x} \underbrace{\begin{pmatrix} \mathbf{0} \\ \boldsymbol{\phi} l_0 \\ \mathbf{0} \\ -\boldsymbol{\phi} l_0 \\ \mathbf{0} \end{pmatrix}}_{\mathbf{f}^j_d} \qquad (3.16)
$$

$\boldsymbol{\phi}\boldsymbol{\phi}^T$ is a 4x4 matrix. The zero matrices in the equation above are of appropriate size so that the $\boldsymbol{\phi}\boldsymbol{\phi}^T$ entries lie in the correct rows and columns corresponding to the whole solution vector $\begin{pmatrix} \mathbf{w}^j_c & \mathbf{w}^j_w \end{pmatrix}^T$. The dropper interaction therefore results in time-variant additional terms of the $\mathbf{B}$ matrix in (3.7) and an additional static force component due to the unstretched dropper length l_0. Rewriting (3.7) with all droppers inside the computational domain gives

$$
\mathbf{A}\mathbf{w}^{j+1} = \left(\mathbf{B} + \sum_i \mathbf{B}^j_{d,i}\right)\mathbf{w}^j + \mathbf{C}\mathbf{w}^{j-1} + \mathbf{f}^j + \sum_i \mathbf{f}^j_{d,i} \qquad (3.17)
$$

Since the dropper positions change with time with respect to the moving coordinate, all dropper input matrices $\mathbf{B}^j_d$ matrices for every dropper have to be calculated anew at each time step and added to the $\mathbf{B}$ matrix.

In the classical non-moving system formulation [3] the handling of droppers is more straight forward and requires less computational effort since their positions are time-invariant. The non-moving system formulation also allows for an easy implementation of the effect of slackening droppers, meaning, that they become inactive when compressed. The difficulties of incorporating slackening droppers in the moving system formulation will be explained later.

When a dropper enters the domain, sudden large dropper forces disturb the solution because the ABCs let waves leave the computational domain freely and do not take into account that an increasingly important restriction in the height difference of contact and carrier wires become active as the dropper approaches the computational boundary. As a simple yet effective countermeasure to smooth those disturbances, the stiffness of the dropper is adjusted with a blending function:

$$
k_d(x_{bd}) = \frac{x_{bd}}{b} - \sin\left(\frac{2\pi x_{bd}}{b}\right)\frac{1}{2\pi} \qquad (3.18)
$$

For $x_{bd} = l - x_d(t)$, $0 \leq x_{bd} \leq b$ denoting the distance between the dropper and the boundary it has entered and b is the width of the blending area after which the dropper stiffness is restored to its full value (see Fig. 3.3). This adjustment of the dropper stiffness helped to decrease high frequency distortions of droppers entering the computational domain.
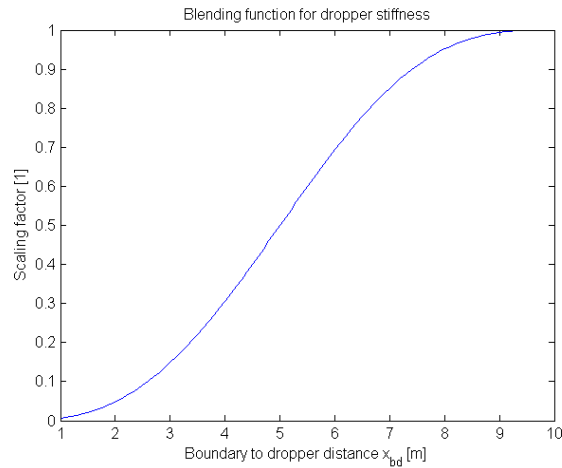
Figure 3.3: Blending function for the dropper stiffness

3.2 Pantograph model

A general discrete state space formulation of the pantograph dynamics can be given by

$$\mathbf{w_p}^{n+1} = \mathbf{f_p}(\mathbf{w_p}^n, F_{\text{cont}}(\mathbf{w_p}^n, \mathbf{w}^n)) \tag{3.19}$$

where $\mathbf{w_p}$ is the state vector of the pantograph and $\mathbf{f_p}$ is a vector function. The contact force F_{cont} is the only source responsible for a coupling of motion of the catenary and the pantograph. If the contact force is explicitly given by the known states of the pantograph and the catenary at the time step n, the discrete state space systems describing the motion of the catenary and the pantograph can be solved separately for the next time step with the contact force as an external input to both systems. This allows a co-simulation of the catenary and interchangeable pantograph models.

In the following, a simple two-mass oscillator will be used as a pantograph model. Its equations of motion are given by

$$\begin{aligned}
m_1 w_{p,1} =& - d_1(\dot{w}_{p,1} - \dot{w}_{p,2}) - c_1(w_{p,1} - w_{p,2}) - F_{\text{cont}} - m_1 g \\
m_2 w_{p,2} =& - d_2 \dot{w}_{p,2} + d_1(\dot{w}_{p,1} - \dot{w}_{p,2}) - c_2 w_{p,2} + \\
& c_1(w_{p,1} - w_{p,2}) + F_0 - m_2 g
\end{aligned} \tag{3.20}$$

where m_n is the mass of body n, g is the gravitational constant, c_1 and d_1 are the spring and damping coefficients between the two masses and c_2 and d_2 the spring and damping between the second mass and the inertial reference frame. F_{cont} is the contact force between the first mass and the contact wire and F_0 is a static force pushing upwards against Body 2 to achieve contact between the pantograph head (Body 1) and the catenary. The contact force is modelled as a unilateral spring which

is only active when compressed:

$$
\begin{aligned}
F_{cont} &= k_{cont}(w_{p,1} - w_w(x_p)) && \text{if } w_{p,1} - w_w(x_p) > 0 \\
F_{cont} &= 0 && \text{if } w_{p,1} - w_w(x_p) \leq 0
\end{aligned}
\tag{3.21}
$$

With the contact force the equations for the catenary (3.17) are extended to

$$
\mathbf{A}\mathbf{w}^{j+1} = \Big(\mathbf{B} + \sum_i \mathbf{B}_{d,i}^j\Big)\mathbf{w}^j + \mathbf{C}\mathbf{w}^{j-1} + \mathbf{f}^j + \sum_i \mathbf{f}_{d,i}^j + \mathbf{f}_{\text{cont}}
\tag{3.22}
$$

3.3 Decoupling of static and dynamic solution

In equation (3.22) the static vectors $\mathbf{f}^j$, where each element consists of the static force density $-\rho_{c/w}A_{c/w}g$, and $\sum_i \mathbf{f}_{d,i}^j$, the static force density of the unstretched dropper length, result in a static displacement of the catenary with respect to a resting coordinate system. With moving coordinates, where the dropper positions change, the static solution is different for every time step, so it is convenient to refer to it as a pseudo-static solution.

When the length of the discrete system is exactly one span of the catenary, a specific pseudo-static solution $\mathbf{w}_0$ from Eq. (3.22) can be obtained by first replacing the absorbing boundary conditions for the carrier wire with Dirichlet boundary conditions so that it is fixed at mast height for the left and the right boundaries. For the contact wire, the absorbing boundary conditions are replaced with periodic boundary conditions. The speed of the pantograph v is set to zero so that the non-moving EBB equations are obtained and the pseudo-static solution can then be calculated by setting

$$
\mathbf{w}^{j+1} = \mathbf{w}^j = \mathbf{w}^{j-1} = \mathbf{w}_0
\tag{3.23}
$$

which leads to

$$
\mathbf{w}_0 = (\mathbf{A} - \mathbf{B} - \sum_i \mathbf{B}_{d,i} - \mathbf{C})^{-1}(\mathbf{f}^j + \sum_i \mathbf{f}_{d,i})
\tag{3.24}
$$

Since only the static displacement of the catenary is of interest, interaction with the pantograph was neglected. The decoupling of the static and dynamic solution and replacing the absorbing boundary conditions for the computation of the static solution is necessary, because with absorbing boundary conditions in place constant forces lead to a continuous drift of the whole catenary, meaning that no static solution can be obtained. In the non-moving system formulation, with only Dirichlet boundary conditions which can exert restoring forces, a decoupling of the static and dynamic solution is not necessary. This leads to an easy implementation of slackening droppers. In the moving system formulation, the slackening of a dropper is a discontinuous change of the static solution.

Fig. 3.4 shows an example static solution of the catenary. The individual unstretched length of each dropper was chosen in such a way to minimize the static sag of the
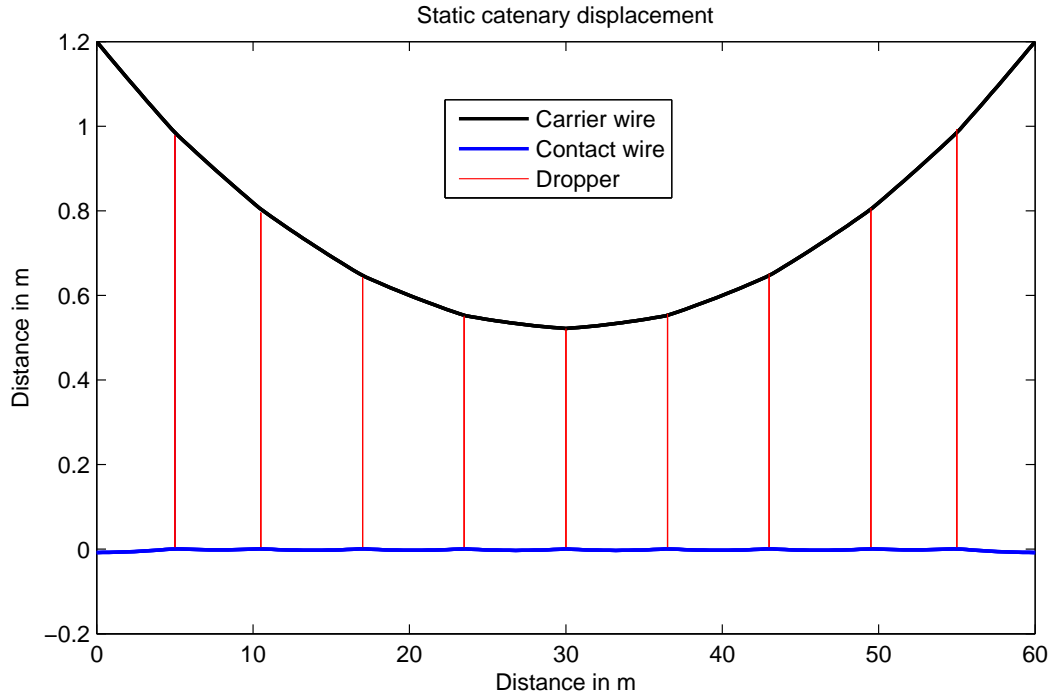
Figure 3.4: Static displacement of the catenary with mast height of $h = 1.2$m, span width $l = 60$m and $i = 9$ droppers

contact wire. The displacement of the contact wire alone is shown in Fig. 3.5. The sag between the droppers causes an excitation of the pantograph.

The static solution computed above is valid for a specific dropper and mast position. Let this be the pseudo-static solution at the start of the computational loop. The pseudo-static solution differs for every time step to come since the catenary is moving through the computational domain. When the travelled distance is equal to the span width the pseudo-static solution is once again equal to that at the beginning. Recomputing the pseudo-static solution at every time instance can be avoided by shifting:

$$w_{0,n}^{j+1}(n\Delta x) = w_{0,n}^j(n\Delta x + \Delta t v) \tag{3.25}$$

This states that the pseudo-static solution at the next time step is obtained by spatially shifting the current pseudo-static solution by $\Delta t v$. Since w_0^j is only known at discrete points, and $n\Delta x + \Delta t v$ lies in general between two grid points, quadratic interpolation is used to calculate the value of the static solution between two discrete points. Once k time steps have passed so that

$$n\Delta x + k\Delta t v \geq (n+1)\Delta x, \tag{3.26}$$
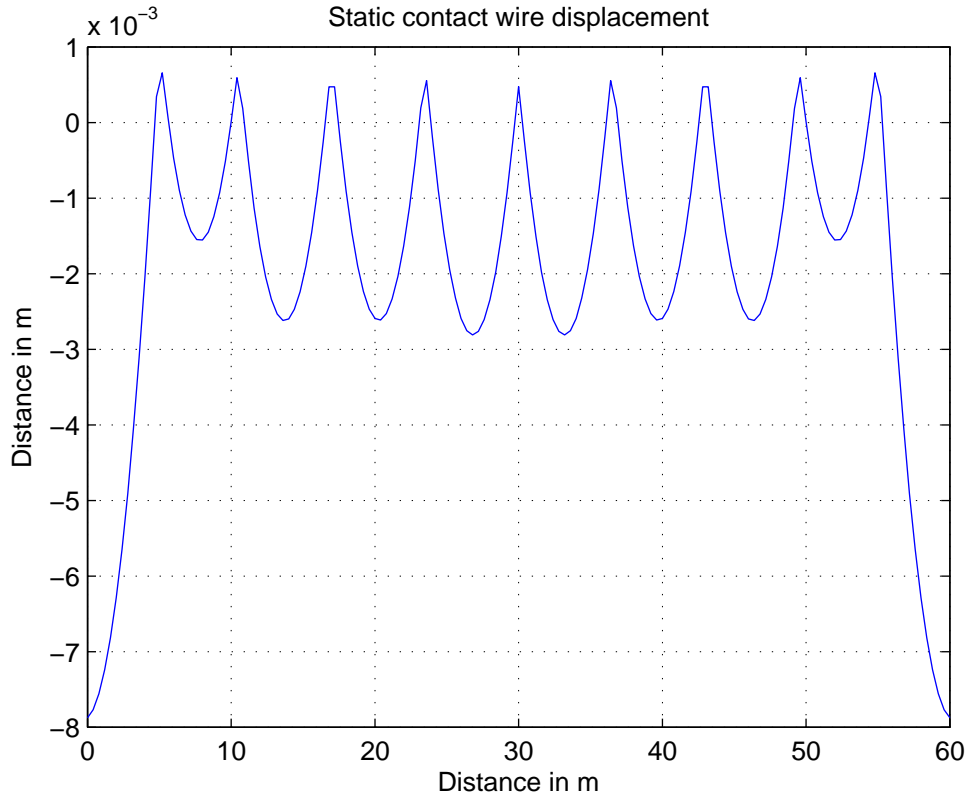
Figure 3.5: Static displacement of the contact wire; span width $l = 60$m and $i = 9$ droppers

the entire static solution can be shifted

$$\mathbf{w}_0^{j+k} = \begin{pmatrix} 0 & 1 & 0 & 0 & \dots \\ 0 & 0 & 1 & 0 & \dots \\ 0 & 0 & 0 & 1 & \dots \\ \vdots & & & & \ddots \\ 1 & 0 & 0 & 0 & \dots \end{pmatrix} \mathbf{w}_0^j \tag{3.27}$$

The static solution now only needs to be computed at the first time step, and for every following step it is obtained by shifting and interpolation. The total solution is then given by

$$\mathbf{w}^j = \mathbf{w}_d^j + \mathbf{w}_0^j \tag{3.28}$$

where $\mathbf{w}_d^j$ denotes only the dynamic solution of the system. It is obtained by evaluating (3.22) with all static forces ($\mathbf{f}^j$, and $\sum_i \mathbf{f}_{d,i}^j$) neglected.

3.4 Computational loop

The necessary steps to start, maintain, and end the computational loop in their correct order are explained here and visualized in Fig. 3.6.

- **Prepare**: At first the time-invariant portions of the system matrices are built. These are essentially the discretized Euler-Bernoulli beam equations for the catenary without added droppers (3.7) and the state space system for the two-mass oscillator pantograph model (3.20). The dropper matrices (3.16) at starting position can be defined and the initial pseudo-static solution is computed (3.24). Absorbing boundary conditions are applied and with the desired initial conditions the computational loop can be started.

- **Computational loop**: Depending on the current states (dynamic and static solution) of the catenary and the pantograph the current contact force is calculated. The dropper matrices valid for the current time step are added. After that, the dynamic solution of the catenary and the pantograph can be updated for the next time step. To easily utilize different (possibly non-linear) pantograph models, the catenary and pantograph states are not aggregated into one system but rather computed separately. The pseudo-static solution for the next time step is obtained by shifting and interpolating and added to the dynamic solution. The time-variant dropper matrices for the next iteration are computed and stored as well as the mast position, for which Dirichlet conditions are applied. The current iteration is now complete and all informations to restart the computational loop are given.

- **Post-processing**: When the exit condition is met, the computational loop is stopped and the generated data can be used for post-processing. The exit condition may be a limitation of iterations (e.g. maximum simulation time), but since in the moving-system formulation the total simulation time does not increase the computational effort per time step, the loop could be continued indefinitely.
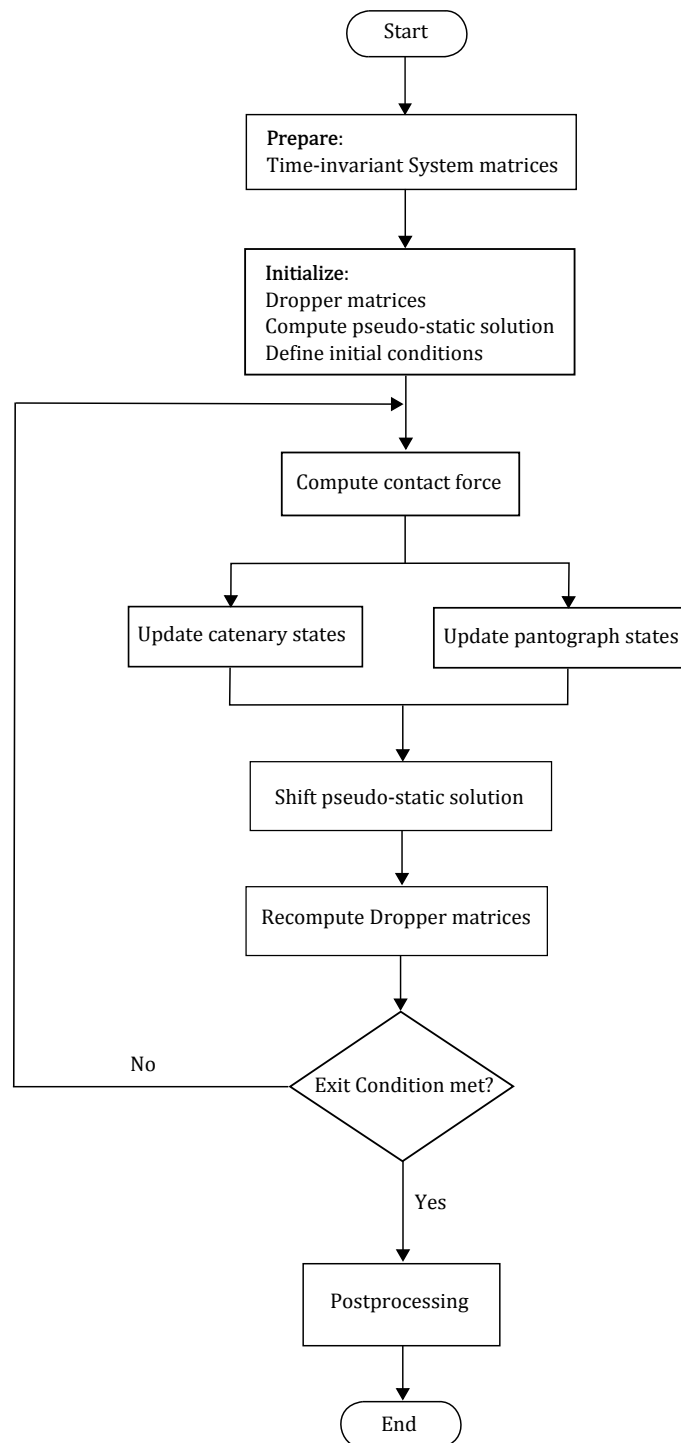
Figure 3.6: Simulation flowchart

Chapter 4

Simulation results

In this chapter, the simulation results of the moving small-scale (SS) system proposed in this work are compared against that of a traditional non-moving large-scale (LS) system, which is described in detail in [3]. All computations are done with the MATLAB software package. As mentioned in the previous chapter, the LS system allows for an easy implementation of slackening droppers, whereas in the SS system this is not straightforward possible because of the decoupled static and dynamic solution. Therefore the effect of slackening droppers is present in the LS system whereas in the SS system it is not.

The parameters for the catenary and the pantograph used in the following simulations are outlined in Tables 4.1 and 4.3. The dropper configuration for the given catenary resulting in a minimal static sag is shown in Table 4.2.

Table 4.1: Catenary parameters

Parameter	Symbol	Value
length of span	l	60 [m]
distance carrier/contact wire	h	1.2 [m]
mass per unit length (carrier)	$\rho_c A_c$	1.07 [kg/m]
mass per unit length (contact)	$\rho_w A_w$	1.35 [km/m]
viscous damping coefficient (carrier)	β_c	0.03 [Ns/m]
viscous damping coefficient (contact)	β_w	1 [Ns/m]
bending stiffness (carrier)	$E_c I_c$	0 [Nm^2]
bending stiffness (contact)	$E_w I_w$	[150 Nm^2]
tensile force (carrier)	T_c	16 [kN]
tensile force (contact)	T_w	20 [kN]
gravitational constant	g	9.81 [m/s^2]
dropper stiffness	k_d	100 [kN/m]

Table 4.2: Dropper configuration

Dropper Nr.	1	2	3	4	5	6	7	8	9
x_d [m]	5	10.5	17	23.5	30	36.5	43	49.5	55
l_0 [m]	0.984	0.803	0.646	0.552	0.520	0.552	0.646	0.803	0.984

Table 4.3: Pantograph parameters

Parameter	Symbol	Value
contact unilateral spring constant	k_{cont}	50 [kN/m]
spring stiffness 1	c_1	50 [N/m]
spring stiffness 2	c_2	4200 [N/m]
damping coefficient 1	d_1	90 [Ns/m]
damping coefficient 2	d_2	10 [Ns/m]
mass 1	m_1	15 [kg]
mass 2	m_2	7.2 [kg]
train velocity	v	250 [km/h]
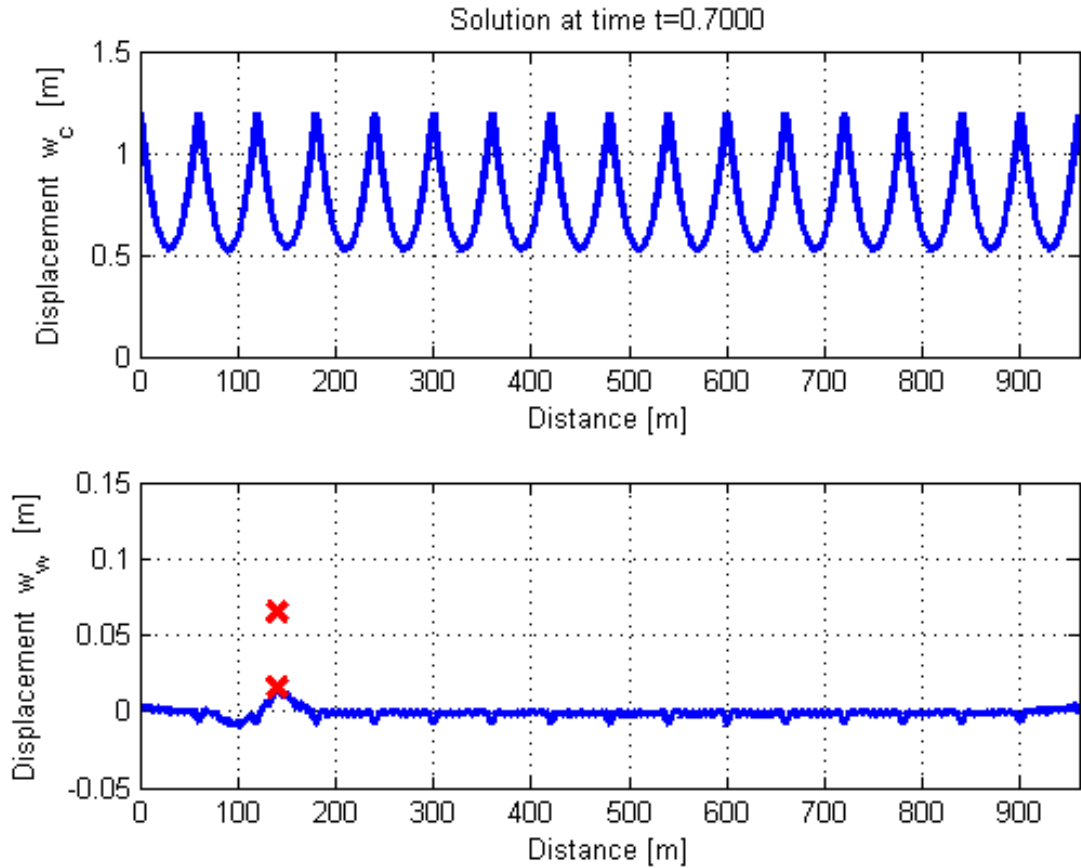
Figure 4.1: Large scale reference system at time instance t=0.7s with a spatial step size of $\Delta x = 0.4$m and a temporal step size of $\Delta t = 7 * 10^{-4}$s

In Fig. 4.1 the solution for the LS System at an arbitrarily chosen time instance is shown. For a constant velocity of $v = 250$ km/h it takes the pantograph 0.864 seconds to pass one span of the catenary. For a simulation time of 10 seconds, the catenary has to be at least 12 spans long. The LS system has 16 spans so reflections at the boundary do not disturb the pantograph. The increased dropper distance at mast position results in the negative peaks of the contact wire. The spatial grid size Δx was chosen to be 0.4 m. In sum, there are 4817 variables to be solved for the catenary. The temporal step size Δt is $7 * 10^{-4}$ s.

4.1 Test case 1: Uplift force of 260 N

The gravitational force of the two masses combined is 217.8 N. In the first test case a constant force $F_0 = 260N$ acting on the second body of the pantograph is applied. This leads to a mean static contact force of 42 N which is generally deemed to low. A typical contact force of 120 N is desired (see [16]).
A comparison of the LS and SS simulation results is shown in Fig. 4.2. The depiction of the LS system is just a cut-out of the total solution seen in Fig. 4.1 and overlaid to be consistent with the moving coordinates, whereas the SS system is fully displayed. Since in the moving formulation the length of the catenary is one span there are only 302 variables for the catenary with $\Delta x = 0.4$ m.
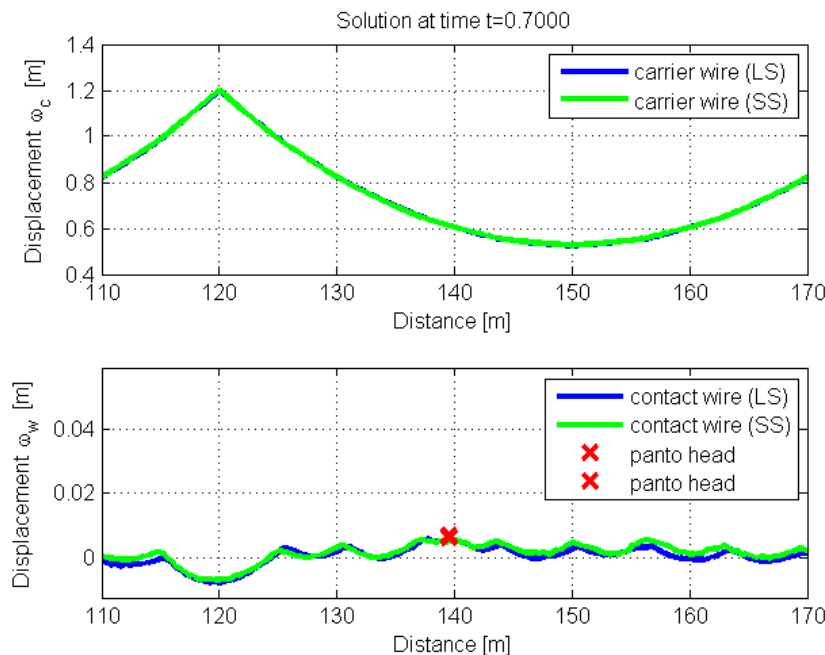

Figure 4.2: Comparison between the LS (blue) and SS (green) system at the time instance t=0.7s.

The pantograph-head displacements are compared in Fig. 4.3. The SS gives a good

approximation of the dynamics although there is a slight overshoot. A period of 0.864s can be observed which is the time it takes for the pantograph to pass one span. The peaks during a period occur when the pantograph currently moves between two droppers.
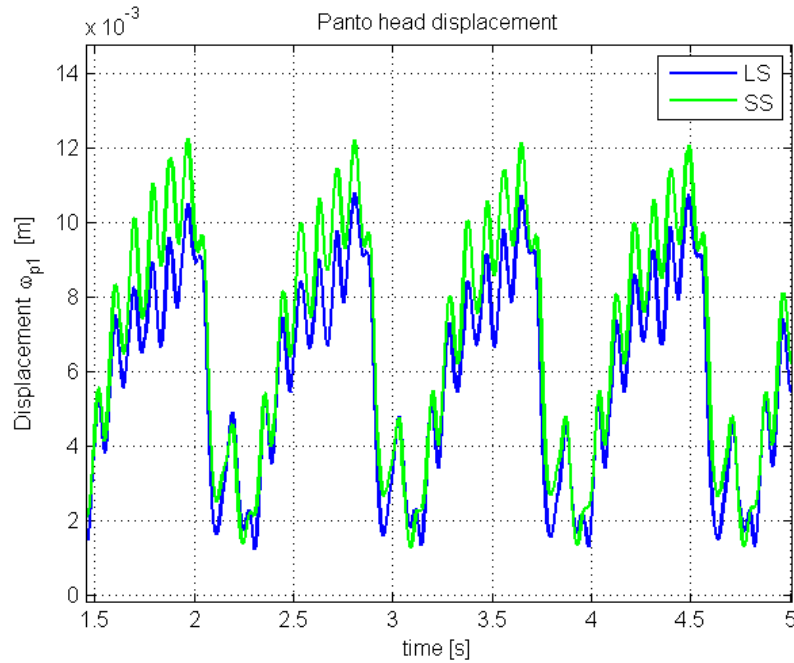

Figure 4.3: Comparison between the pantograph-head displacement for the LS (blue) and the SS (green) system.

To quantify the goodness of fit of the pantograph-head displacement, the normalized mean square error is used.

$$fit = 1 - \left\| \frac{\mathbf{x} - \mathbf{x}_{ref}}{\mathbf{x} - mean(\mathbf{x}_{ref})} \right\|^2 \tag{4.1}$$

where $\mathbf{x}$ is the signal under test compared to the reference signal $\mathbf{x}_{ref}$. The fit varies between $-\infty$ (bad fit) and 1(perfect fit). For the simulation above, a fit between the SS and LS pantograph-head displacement of 0.86 is achieved.
The contact force is modelled as a unilateral spring with a spring constant of $k_{cont} = 50$ kN/m. Therefore there are high frequency oscillations in the contact force. In [16] it is stated, that the frequency range of interest is between 0-20 Hz. A zero phase distortion low-pass filter is used to process the raw contact force data. In Fig. 4.4 the filtered contact forces between the pantograph and the catenary for the LS and SS system are compared. As a result of the low static force contact loss can be observed. The fit of the contact forces amounts to 0.66.
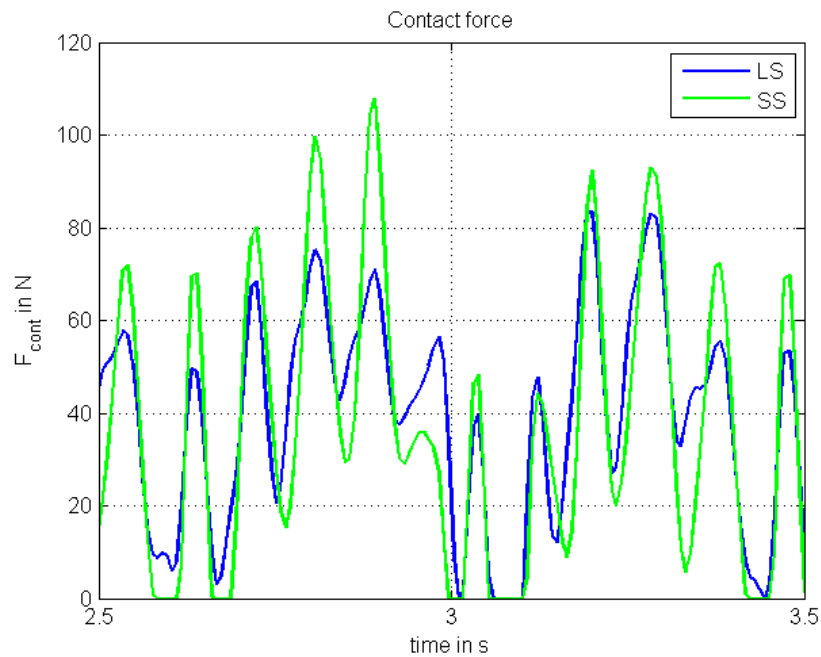
Figure 4.4: Comparison of the filtered contact force between catenary and pantograph-head for the LS (blue) and the SS (green) system.

Fig. 4.5 shows the power spectral density for both systems in the range of interest. The first peak around 1.2 Hz is the span width frequency. The increase of the power density at a frequency of 10.4 Hz is due to the droppers.

Overall, a good fit between the SS and LS system can be observed with the SS system having a much faster computation time. In this test case, the simulation time was set to 10 seconds. The runtime for the LS system was 90.1s, whereas the runtime for the SS system was 14.9s. The computations were done on a personal laptop computer (i8-4702MQ @ 2.20Ghz CPU, 8GB RAM).
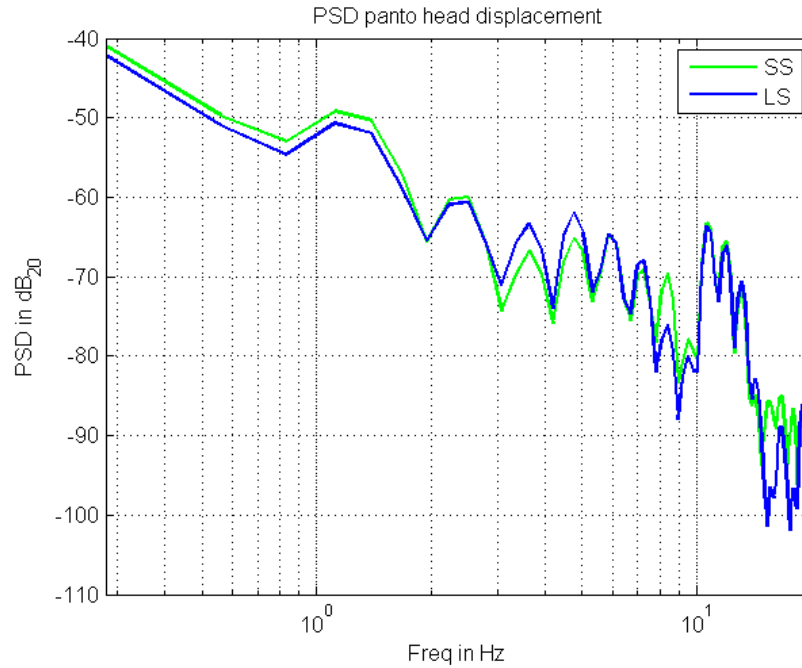
Figure 4.5: Power spectral density of the LS (blue) and SS (green) System.

4.2 Test case 2: Uplift force of 340 N

In the second test case, the catenary and pantograph parameters are the same as in the first one, but the uplift force of to pantograph is increased to 340N. This results in a mean static contact force between pantograph and catenary of 121N. The pantograph-head displacement is shown in Fig. 4.6. The overall dynamic is approximated well, but the overshoot compared to the LS system increases with a higher uplift force. One reason for this is that in the SS system the absorbing boundary conditions don't exert any restoring forces. Only the Dirichlet boundary condition on the carrier wire at mast position keeps the whole catenary from drifting away. When the mast leaves the computational domain on one side, the tie-down suddenly disappears since no information outside the computational domain is used and the carrier wire can move freely. A similar problem occurs when the mast enters the computational domain. Suddenly a constraint on the carrier wire is enforced. This rapid pull down of the carrier wire results in a wave travelling over the pantograph for which the contact force decreases to the point of contact loss, see Fig. 4.7. The distortion of the system by an incoming mast can also be seen by plotting the fit of the contact wire for the SS in reference to the LS system over time (Fig. 4.8). The pantograph-head fit is at 0.6 which is worse then the fit for the simulation with a lower uplift force. The higher the uplift force the greater the incoming mast distortion.
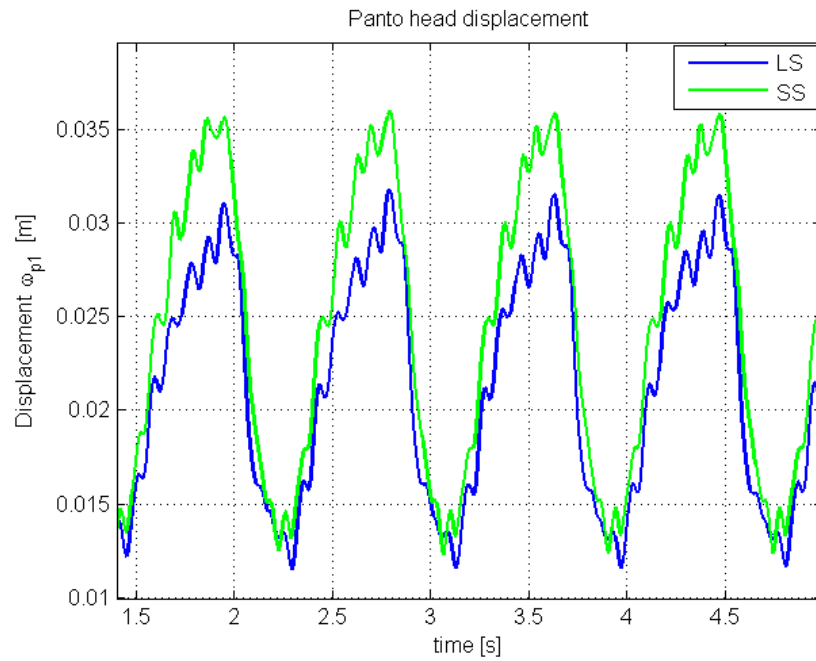
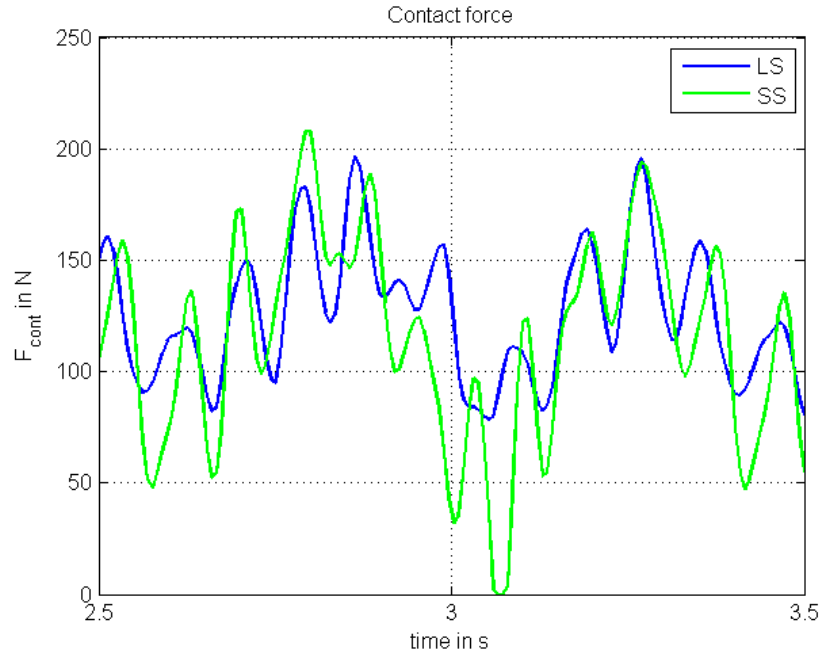Figure 4.6: Power spectral density of the LS (blue) and SS (green) System.

Figure 4.7: Filtered contact force for the LS (blue) and SS (green) system.
At 3.1s a decrease of the SS contact force can be observed which
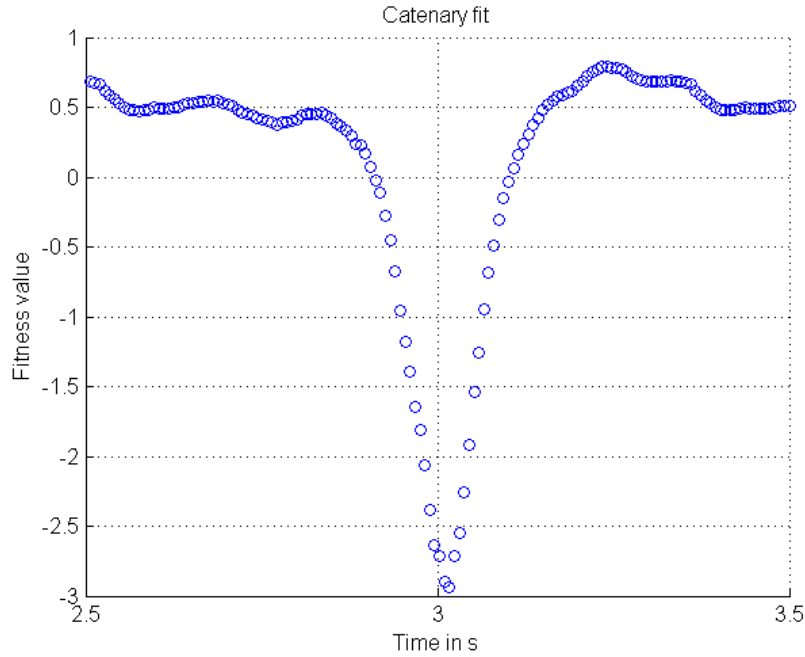occurs due to the distortion of an entering mast

Figure 4.8: Fit of the contact wire for the SS in reference to the LS system. The distortion of an incoming mast drastically decreases the overall fit of the contact wire.

4.3 Test case 3: Elastically constrained contact wire boundaries

As seen in the previous test case, the freely moving absorbing boundary of the contact wire combined with the event of an incoming mast results in a distortion of the solution. One possible way to incorporate the restoring effect of the mast is investigated in this test case. On the boundaries of the carrier wire springs with a variable stiffness are applied. To get the variable stiffness function, the equivalent stiffness of the carrier wire is determined. For that, a constant force is applied to every node of the carrier wire and the static displacement is calculated (for the carrier wire only). If repeated for a second constant force, two static displacement fields are obtained for which the varying contact stiffness can be determined by

$$\Delta \mathbf{w}_{c,0} = \mathbf{k}(x)\Delta F \tag{4.2}$$

where $\Delta \mathbf{w}_{c,0}$ is the difference between the two static displacement fields and ΔF is the force difference. The equivalent variable stiffness of the carrier wire is shown in Fig. 4.9. The infinite stiffness at mast position is removed to avoid numerical difficulties (the spring at the boundary is overruled anyway by the Dirichlet condition when the mast is currently at boundary position)
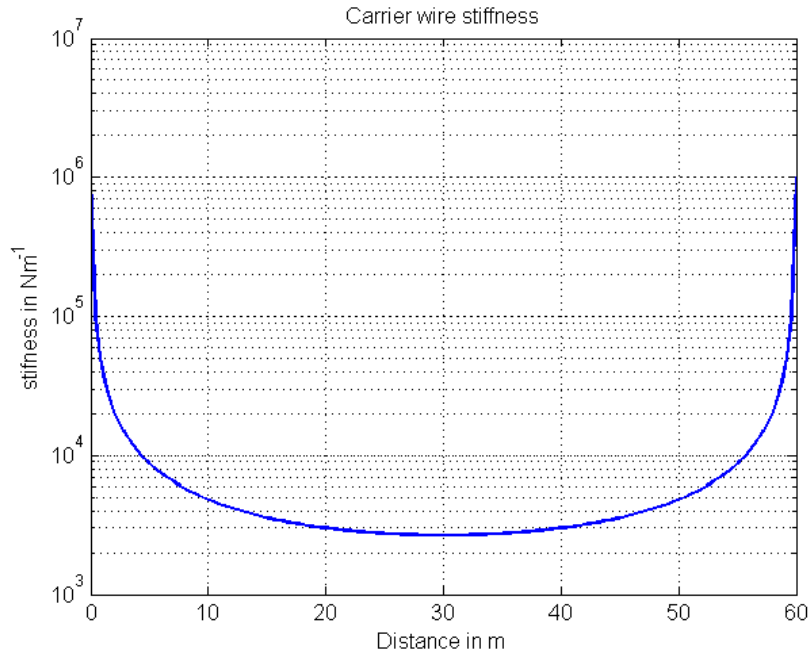
Figure 4.9: Equivalent variable stiffness of the carrier wire. A logarithmic scale is used for the Y-axis

The spring at boundary position alters the catenary dynamics and therefore the pantograph-head solution, see Fig. 4.10. An additional decaying transient behaviour can be observed, but also the overshoot is diminished. Due to the variable springs the pantograph-head fit is 0.35, which is less then in the previous test case. By looking at the contact force (Fig. 4.11), it can be seen that the distortion of the wave generated by the mast entering the computational domain was removed. In Fig. 4.12the contact wire fit over time is shown. A comparison with Fig. 4.8 yields, that adding the variable springs has also helped to increase the overall fit of the contact wire.

Clearly the added springs at the boundary are too simple for an approach and they alter the solution of the pantograph-head displacement in an unwanted way. But this simple test case shows, that some additional boundary constraints are desired and can help to improve the overall performance of the SS system approach.
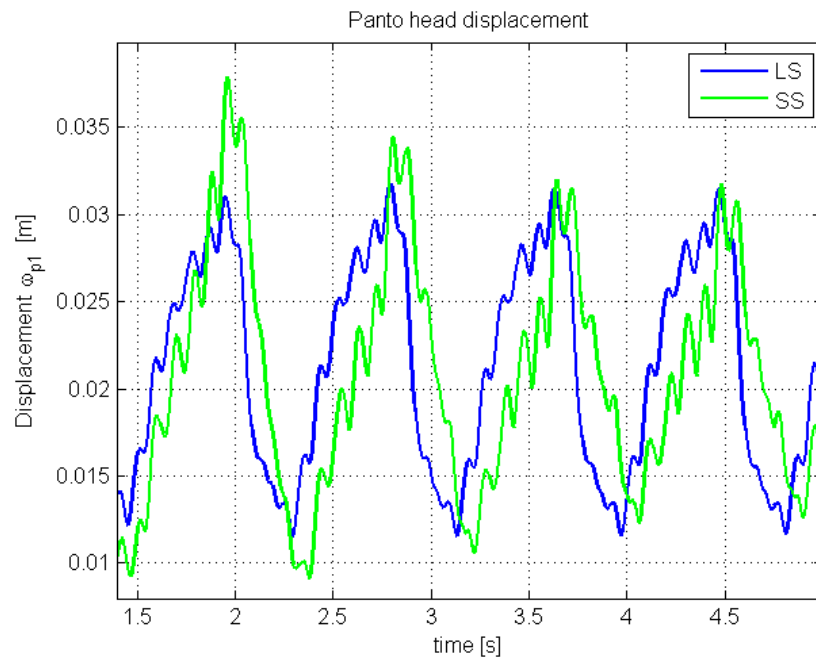
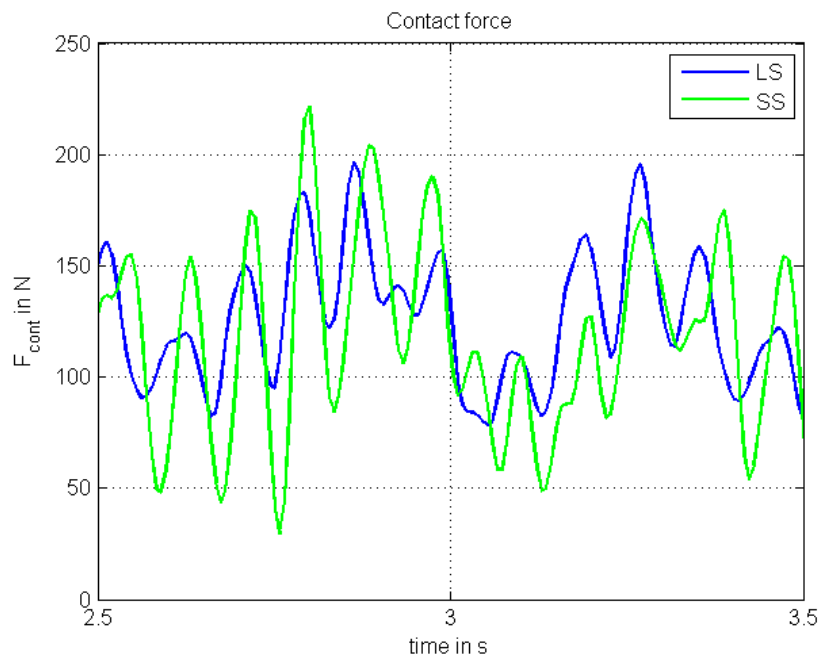Figure 4.10: Pantograph-head displacement with a variable spring at boundary position for the SS system

Figure 4.11: Comparison of the contact force with added variable spring at boundary position for the SS system
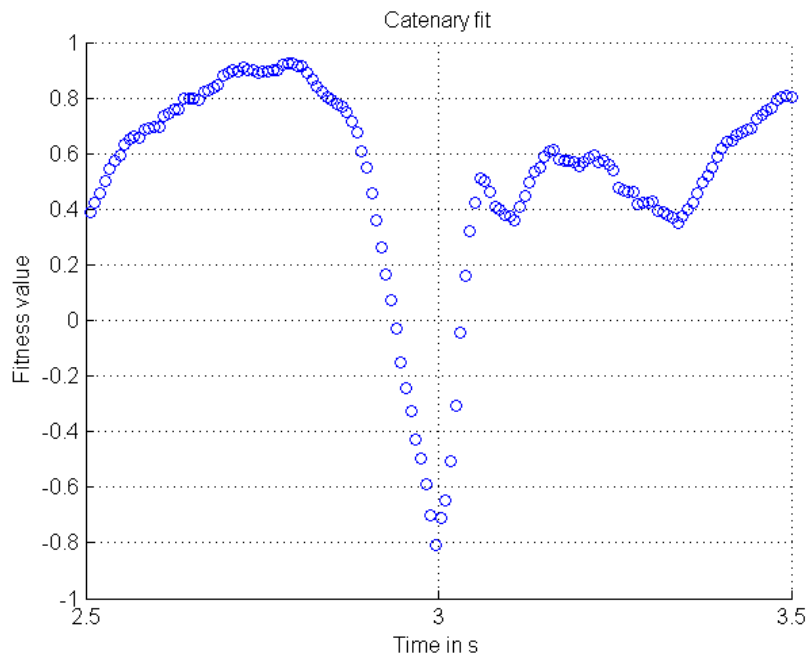
Figure 4.12: Fit of the contact wire with added variable springs at boundary position for the SS system
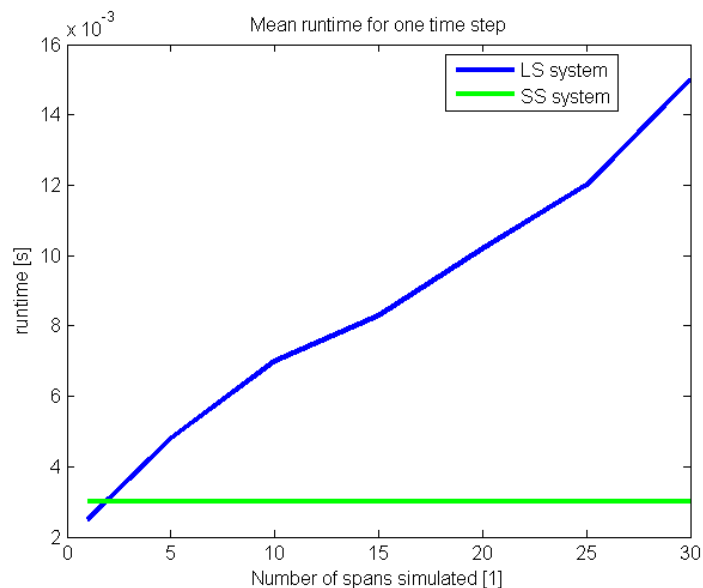
Chapter 5

Conclusion

Figure 5.1: Continuously increasing mean runtime subjected to the number of spans for the LS system (blue) compared to the constant mean runtime for the SS system (green)

The transformation of the coupled catenary and pantograph dynamics to a moving coordinate and introducing absorbing boundary conditions led to a lean formulation of the problem where the computational domain is only of the length of one span of the catenary. This greatly reduces the number of variables that have to be calculated each time step, increasing computational efficiency. Furthermore, the length of the moving small-scale system is independent of the simulation time, which is not the case for a traditional non-moving system formulation. In other words, the runtime for one time step is constant for any desired simulation time whereas in the non-moving system formulation the runtime continuously increases with the simulation time since the length of the system has to be increased accordingly. In Fig. 5.1

the mean runtime of the LS system for one time step is plotted over the number of spans that are simulated. If the SS and the LS system are both of the length of one span, the LS system has a faster mean runtime because the transformation to moving coordinates lead to fully populated discrete system matrices whereas in the non moving formulation the discrete system matrices are sparse. After a length of two spans the advantage of reduced variables outweighs the sparsity of the system matrices.

The simulation error between the small-scale and the large scale system formulation can be traced back to two main factors

1. The absorbing boundary conditions are only perfect if the discrete wave equation is dispersion free. Since for the Euler-Bernoulli beam there is always dispersion only waves with a phase speed close to the pseudo-velocity $c = \sqrt{\frac{T}{\rho A}}$ are absorbed which are typical waves with a low wave number. The greater the difference between phase speed and pseudo-velocity the worse the absorption of that particular wave.

2. Currently there is no information outside of the computational domain incorporated into the simulation. Incoming masts and droppers impose a discontinuous constraint on the contact and carrier wire inducing distortion waves.

Future work to counter those problems is to find a suitable boundary control that is able to absorb waves within a dispersive medium without adding too much computational effort. This can be done by rewriting the absorption properties of a perfectly matched layer as an optimization problem to find a state-space controller that mimics the behaviour. Thus no additional auxiliary fields are necessary.
As it was shown in test case 3 in the previous chapter, the assumption of total absorption at the boundary and therefore a free wave solution outside the computational domain is not entirely justified as droppers and masts that left the domain or are about to enter it do have an effect on the boundary. Certain appropriate additional constraints are desired to improve the accuracy of the small-scale system formulation.

Bibliography

[1] G Poetsch, Je Evans, R Meisinger, W Kortüm, W Baldauf, A Veitl, and J Wallaschek. Pantograph/catenary dynamics and control. *Vehicle System Dynamics*, 28(2-3):159–195, 1997.

[2] Steven G Johnson. Notes on perfectly matched layers (pmls). *Lecture notes, Massachusetts Institute of Technology, Massachusetts*, 2008.

[3] M Arnold and B Simeon. Pantograph and catenary dynamics: a benchmark problem and its numerical solution. *Applied Numerical Mathematics*, 34(4):345–362, 2000.

[4] J Pombo, J Ambrósio, M Pereira, F Rauter, A Collina, and A Facchinetti. Influence of the aerodynamic forces on the pantograph–catenary system for high-speed trains. *Vehicle System Dynamics*, 47(11):1327–1347, 2009.

[5] A Facchinetti and S Bruni. Hardware-in-the-loop hybrid simulation of pantograph–catenary interaction. *Journal of Sound and Vibration*, 331(12):2783–2797, 2012.

[6] Weihua Zhang, Guiming Mei, Xuejie Wu, and Zhiyun Shen. Hybrid simulation of dynamics for the pantograph-catenary system. *Vehicle System Dynamics*, 38(6):393–414, 2002.

[7] Bertil Gustafsson, Heinz-Otto Kreiss, and Joseph Oliger. *Time-dependent problems and difference methods*, volume 121. John Wiley & Sons, 2013.

[8] Hans Petter Langtangen. *Finite difference methods for wave motion*. 2013.

[9] Gerald Beresford Whitham. *Linear and nonlinear waves*, volume 42. John Wiley & Sons, 2011.

[10] Robert L Higdon. Numerical absorbing boundary conditions for the wave equation. *Mathematics of computation*, 49(179):65–90, 1987.

[11] Björn Engquist and Andrew Majda. Absorbing boundary conditions for numerical simulation of waves. *Proceedings of the National Academy of Sciences*, 74(5):1765–1766, 1977.

[12] Laurence Halpern. Absorbing boundary conditions for the discretization schemes of the one-dimensional wave equation. *MATHEMATICS of computation*, 38(158):415–429, 1982.

[13] Jean-Pierre Berenger. A perfectly matched layer for the absorption of electromagnetic waves. *Journal of computational physics*, 114(2):185–200, 1994.

[14] Marcus J Grote. Nonreflecting boundary conditions for time dependent wave propagation. ETH, Seminar für Angewandte Mathematik, 2000.

[15] F ARBABI and MS FARZANIAN. Propagation of waves in infinite beams: Pml approach.

[16] EN DIN. 50318 (2003-04) bahnanwendungen–stromabnahmesysteme–validierung von simulationssystemen für das dynamische zusammenwirken zwischen stromabnehmer und oberleitung. *Deutsche Fassung EN*, 50318, 2002.